Optical Materials: X 18 (2023) 100238

Contents lists available at ScienceDirect

Optical Materials: X

journal homepage: www.journals.elsevier.com/optical-materials-x

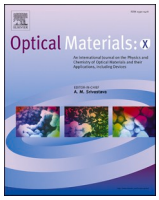

Recent progress in lanthanide-based metal halide perovskites: Synthesis, properties, and applications

Tuhin Samanta [a], Nagaraju Mukurala [a], Noolu Srinivasa Manikanta Viswanath [a], Joo Hyeong Han [a], Han Bin Cho [a], Jeong Wan Min [a], Sung Woo Jung [a], Yongmin Park [a], Woon Jin Chung [b,**], Won Bin Im [a,*]

[a] Division of Materials Science and Engineering, Hanyang University, 222 Wangsimni-ro, Seongdong-gu, Seoul, 04763, Republic of Korea
[b] Institute for Rare Metals and Division of Advanced Material Engineering, Kongju National University, 1223-24, Cheonan-daero, Seobuk-gu, Cheonan, Chungnam, 31080, Republic of Korea

A B S T R A C T

Metal halide perovskites (MHPs) have recently attracted significant interest, owing to their excellent optoelectronic properties and diverse applications, including photovoltaics, solid-state lighting emitting diodes (LEDs), and other optoelectronic applications. However, owing to the toxic nature of lead-based MHPs, lanthanide-based MHPs have recently emerged as an alternative, leading to new opportunities for emerging applications, such as in near-infrared (NIR) imaging, NIR cameras, white LEDs, photovoltaics, and information encryption. Moreover, lanthanide doping significantly enhances the stability and optical properties of MHPs. In this review, we have attempted to overview state-of-the-art synthesis strategies and investigate the structural, and optical properties of MHPs. Furthermore, several applications of MHPs, white LEDs, solar cells, and temperature sensors are discussed along with outlooks and future directions.

1. Introduction

Metal halide perovskites (MHPs) have attracted wide attention over the last two decades owing to their outstanding optoelectronic properties, and potential applications in optoelectronics [1–5]. MHP nanocrystals (NCs) exhibit interesting optical properties such as high color purity with near unity photoluminescence quantum yields (PLQY), and high electron-hole recombination rates [6–9]. Generally, perovskites have a chemical composition of ABX_3, where A occupies the corner position, B is the body-centered position, and X is the face-centered positions. The A (cuboctahedral) and B (octahedral) cations are coordinated at 12 and 6 X, respectively. The structural stability of perovskites depends on the Goldschmidt tolerance factor "t" and octahedral factor (μ) as follows [10]:

$$t = \frac{(r_A + r_X)}{\sqrt{2}(r_B + r_X)}$$

$$\mu = \frac{r_B}{r_X}$$

where r_A, r_B, and r_X denotes the ionic radii of A, B, and X, respectively. To form the stable three-dimensional (3D) perovskite structure, 't' should be between 0.8 and 1. Additionally, the octahedral factor should be in the range of $0.44 \leq \mu \leq 0.90$. The crystal structure of perovskite is expected to form a cubic structure when 't' is in the range of 0.9 to 1, whereas at $t = 1$, perovskite forms an ideal cubic structure. Perovskite forms orthorhombic or tetragonal or rhombohedral crystal structures when 't' lies between 0.8 and 0.89. For $t > 1$, MHP tends to crystallize in a hexagonal structure wheras an orthogonal MHP is preferred in cases where $t < 0.8$. Fig. 1 illustrates the structural changes with respect to the tolerance factor. In the ABX_3 MHPs, A is a monovalent cation (Cs^+, Na^+, etc.), B is divalent (Pb^{2+}, Sn^{2+}, Ge^{2+}, etc.), and X is a halide (Cl^-, Br^-, and I^-) anion [11]. $CsPbX_3$ NCs have been extensively studied because of their excellent optoelectronic properties [12–15]. Furthermore, hybrid perovskites where A is an organic cation ($CH_3NH_3^+$, $CH(NH_2)_2^+$, etc.) have attracted more attention than $CsPbX_3$ because of to their high defect tolerance, long molar absorption, long carrier diffusion length, high PLQY, and wide color tunability [16,17]. However, the chemical stability of hybrid MHPs is a major concern, and their optical properties can be improved for device applications [18]. Additionally, all inorganic MHPs NCs exhibit poor moisture and heat stability, and lead is toxic in nature, which limits their use in commercial applications [19–21]. Hence, in the past few years, materials scientists have developed several lead-free MHPs that exhibit excellent optoelectronic properties [22–25].

* Corresponding author.
** Corresponding author.
E-mail addresses: wjin@kongju.ac.kr (W.J. Chung), imwonbin@hanyang.ac.kr (W.B. Im).

https://doi.org/10.1016/j.omx.2023.100238
Received 31 March 2023; Accepted 20 May 2023
Available online 1 June 2023

However, the optical properties of lead-free MHPs differ from those of lead-halide perovskites (LHPs). Therefore, new synthesis protocols and materials must be developed to resolve this issue.

In this regard, a promising alternative is the use of lanthanide-based MHP NCs because of their unique optical properties, such as a narrow emission band, long photoluminescence (PL) lifetimes, and large stokes/antistokes shifts. Lanthanides have been widely investigated as optically active dopants [26–28]. For instance, lanthanide-based fluoride materials have been extensively studied over the last two decades [29–31]. Interestingly, the octahedral coordination of MHP NCs makes them well suitable for Ln^{3+} doping [32,33]. In Ln^{3+} doped MHPs NCs, Ln^{3+} provide several energy levels within the bandgap of the NCs. Therefore, Ln^{3+} doping produces optical transitions at wavelengths higher than the fundamental absorption range. Typically, Ln^{3+} ions exhibit forbidden *4f-4f* transitions with well-defined energy levels that are approximately constant irrespective of the host material, owing to the shielding effect of the *4f* orbitals. Thus, Ln^{3+} based MHPs exhibit high PL lifetimes, narrow PL, and low absorption coefficient (~1–10 $M^{-1}cm^{-1}$). It is worth noting that Ce^{3+}, Eu^{2+}, and Yb^{2+} ions undergo highly efficient dipole-allowed transitions due to *4f*-5*d* orbital coupling. Additionally, MHP NCs with very high absorption coefficients can sensitize Ln^{3+} ions to induce luminescence [34,35]. In recent years, lead-free MHP NCs such as $CsYbI_3$ NCs, $CsEuCl_3$ NCs, and $Cs_2NaLnCl_6$ NCs + have gained attention, and exhibit promising optical properties similar to LHPs [36–39]. Hence, lanthanide offers an interesting alternative to lead-free MHPs.

Recent years have witnessed the increasing popularity of lanthanide-based MHPs, and a great deal of progress has been made so far, but still enormous efforts are needed to advance further. In this review, we have discussed recent developments in colloidal synthesis methods that incorporate different types of lanthanides doping. We also discuss the stability of MHP NCs via lanthanide doping and their applications. Our review is structured into five main sections: (a) A brief introduction to lanthanide doping in MHPs to offer an insight into their chemical nature, crystal structures, and optical properties. (b) A detailed explanation and analysis of the colloidal synthesis of lanthanide-based MHPs to provide a comprehensive overview of the different synthesis routes. (c) We provide a detailed summary of the stability of MHP NCs via lanthanide doping. (d) The optical properties of lanthanide-based NCs based on MHPs are discussed in the following section. (e) The next section discusses applications of lanthanide-doped MHPs, which perticularly feature the solid-state lighting (SSL) application. Finally, a summary and perspective will be discussed at the end of this review.

2. Synthesis of lanthanide-based MHPs

There are various reports on the synthesis of high-quality MHP NCs in terms of size, morphology, and optical properties, and the focus has been on developing reliable and straightforward approaches. These strategies can be classified as “top-down” and “bottom-up.” The “top-down” synthesis involves fragmentation of bulk materials to nanomaterials mechanically or chemically, whereas the “bottom up” process starts with ions and molecules and proceeds in gas or liquid phase chemical processes. In this article, we discuss the bottom-up synthesis of MHPs. Among the bottom-up methods, hot injection and ligand-assisted reprecipitation (LARP) have been extensively reported. Lanthanide-based MHP NCs are synthesized using a similar technique. Additionally, thin-film synthesis of lanthanide-based MHP has been widely reported for optoelectronic applications such as in photovoltaics and light emitting diodes (LEDs).

2.1. Hot injection method

The hot injection method was first developed in 1993 by Murry and co-worker for the synthesis of quantum dots [40]. The method is based on rapid injection of a precursor into the hot solution of other precursors, surfactants, and high boiling solvents [41,42]. Subsequently, rapid nucleation occurs, leading to the formation of small nuclei. Once nucleation occurs, homogeneous diffusion-controlled growth is observed across the solution. As the growth progresses, Ostwald ripening occurs, in which the larger nanocrystals continue to grow, while the smaller quantum dots dissolve due to their higher chemical potential. Until the saturation point, the average particle size increases, and the concentration of the particles decreases. A schematic of the hot-injection synthesis of MHP NCs is shown in Fig. 2. The hot-injection method is the most effective because it offers control over the size of the particles and size distribution by permitting rapid nucleation, separated from the growth stage. The size and morphology of the NCs are tuned by changing the reaction temperature, time, and precursor concentration. Furthermore, this method has been recognized as effective for the synthesis of various types of NCs. Protesescu et al. synthesized colloidal $CsPbX_3$ (X = Cl, Br, I) NCs using the hot-injection method [6]. $CsPbX_3$ NCs were synthesized by injecting Cs-oleat precursor into a hot solution (140–200 °C) of PBX_2, dissolved in octadecene (ODE), carboxylic acid, and primary amines. A monodisperse size distribution of NCs was

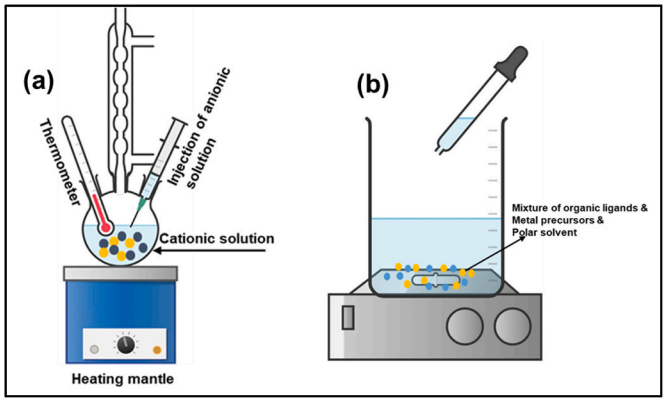

Fig. 2. Schematic of colloidal MHP NCs synthesis method by (a) hot injection (b) ligand assisted reprecipitation.

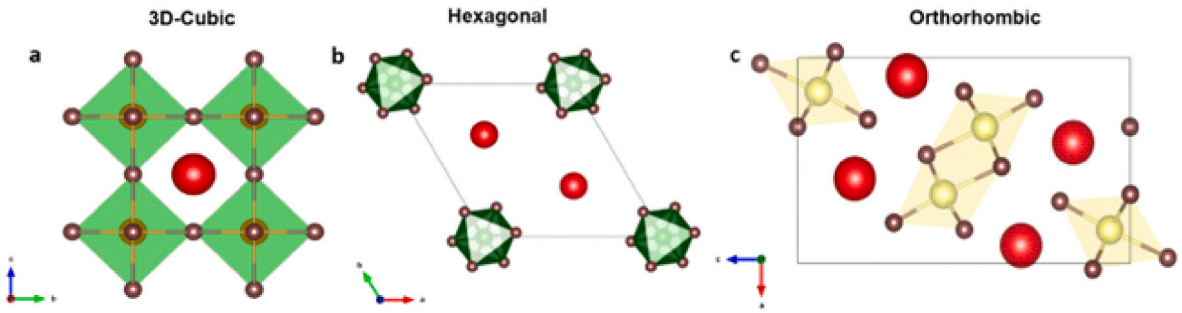

Fig. 1. Formation of (a) cubic, (b) hexagonal, and (c) orthorhombic phased MHPs NCs for different values of the Goldschimt factor (t).

observed for equal amounts of amines and acids. The size of the NCs can be tuned by changing the reaction temperature. Zhang et al. synthesized stable and size-tunable $CsPbBr_3$ NCs using oleylphosphonic acid (OLPA) [43]. OLPA has higher solubility in nonpolar solvents than in other phosphonic acids with linear alkyl chains. Therefore, NCs were synthesized at a low temperature (100 °C). The size of the NCs was tuned in the range 5–10 nm. Lanthanide-doped $CsPbX_3$ NCs were synthesized using the hot-injection method. In 2016, Pan et al. investigated the role of acid, base, and cesium precursors in the colloidal synthesis of CsPbBr3 NCs.

[44]. As shown in Fig. 3, size and shape of the NPs depends on the chain length of carboxylic acid and amine along with temperature. In 2017, Zhou and co-worker reported synthesis of lanthanide (Yb^{3+},Ce^{3+}, Er^{3+}) doped $CsPbCl_3$ using mixture of octadecene and oleic acid by modified hot injection process [45]. Subsequently, Pan et al. have synthesized various lanthanide ions (Ce^{3+}, Sm^{3+}, Eu^{3+}, Tb^{3+}, Dy^{3+}, Er^{3+}, and Yb^{3+}) doped $CsPbCl_3$ MHP NCs via hot-injection method [46]. In a typical hot-injection method, lanthanide chloride and lead chloride are dissolved in a mixture of ODE, oleylamine (OLA), and OA at 160 °C. Subsequently, Cs-oleate was swiftly injected into the solution at 240 °C, and the reaction was stopped after 30 s. Therefore, tetragonal-phased lanthanide-doped $CsPbCl_3$ NCs were formed with uniform cubic particles (Fig. 4). The average size of the NCs decreased with increasing atomic number of the lanthanides. Similarly, Yu et al. have synthesized $CsPbCl_3$:Yb^{3+}, $CsPbCl_3$:Er^{3+}, and $CsPbCl_3$:Yb^{3+}/Er^{3+} NCs via modified hot-injection method [47]. In this method Yb^{3+} ions were successfully doped into the crystal structure of the $CsPbCl_3$ NCs. A uniform cube-shaped with ~10 nm particle size of $CsPbCl_3$ and $CsPbCl_3$:Yb^{3+} NCs were formed. Furthermore, Yb^{3+} doped $CsPbCl_3$ NCs were synthesized via hot injection method using all metal-oleate salts as cation precursors and trimethylchlorosilane (TMS-Cl) as the anion precursor in synthesis [48]. As a result, NCs were formed with better crystallinity and a uniform particle size of 15 nm were formed. Recently, Jin et al. reported a hot-injection method of synthesizing Eu^{2+}-doped $CsPbBr_3$ NCs. Cs-oleate solution was rapidly injected into a solution of $EuBr_2$ into $PbBr_2$ at 200 °C. The morphology of Eu^{2+} doping in $CsPbBr_3$ NCs was cube-shaped, with an average particle size of 8 nm [48].

The synthesis of lanthanide-doped $CsPbX_3$ was similar to that of the undoped $CsPbX_3$ NCs. However, lanthanide-doped $CsPbX_3$ NCs are generally synthesized at higher temperatures than that for the undoped $CsPbX_3$. A list of the lanthanide-doped MHP NCs is presented in Table 1.

The search for lead-free MHP NCs is of great interest owing to the toxicity of lead. Recently, several lead-free (Bi, Cu, Sn, and Sb) MHP NCs have been reported [49]. However, reported lead-free MHPs exhibit poor optical properties compared to the $CsPbX_3$ NCs and moreover finding a new materials alternative to $CsPbX_3$ remains challenging. Recently, Moon et al. fabricated cesium ytterbium triiodide ($CsYbI_3$) MHP NCs using a hot-injection technique [38]. In the typical hot-injection method, YbI_2 was dissolved in an ODE solvent and heated at 120 °C under vacuum for 150 min. Subsequently, OLA and OA were added to the solution. Subsequently, Cs-oleate solution was injected swiftly into the YbI_2 solution at 180 °C. Cubic-phased $CsYbI_3$ NCs with high crystallinity were formed, as shown in Fig. 5a. Notably, the NCs were formed with a uniform particle size distribution of 9.5 nm (Fig. 5b). Another lanthanide-based lead-free MHP is $CsEuCl_3$ NC, which has been synthesized using a hot-injection method [37]. In this synthesis method, Eu^{3+} ($EuCl_3$) was reduced to Eu^{2+} by heating $EuCl_3$ in OLA at 300 °C for 30 min. OLA was used as a reducing agent, and subsequently, $EuCl_3$ was mixed with ODE, OLA, and TOP and heated at 120 °C under vacuum. Thereafter, Cs-oleate solution was injected into the above solution at 250 °C. After 45 min, the reaction was quenched in an ice water bath. To obtain NCs, the solution was centrifuged with hexane or toluene. A pure-phased tetragonal crystal structure with homogeneous size distribution of the NCs at approximately 15 nm was formed. The schematic of $CsEuCl_3$ NCs synthesis along with unit cell structure, XRD pattern and TEM image are shown in Fig. 6.

Lanthanide-based lead-free double-perovskite (DP) NCs are another promising alternative to $CsPbX_3$ NCs. Recently, Sun et al. reported the synthesis of Cs_2NaLnX_6 (Ln = La, Ce, Sm, Eu, Tb, Er, Yb; X = Cl, Br, I) double metal halide perovskites (DMHP) NCs using a hot-injection method [39]. In the typical method, cesium acetate (CsOAc), sodium acetate (NaOAc), lanthanide acetate ($Ln(OAc)_3$) were dissolved in a mixture of ODE, OA, and OLA at 140 °C under vacuum. Subsequently, the solution was heated at 250 °C, and TMS-Cl was injected swiftly. As

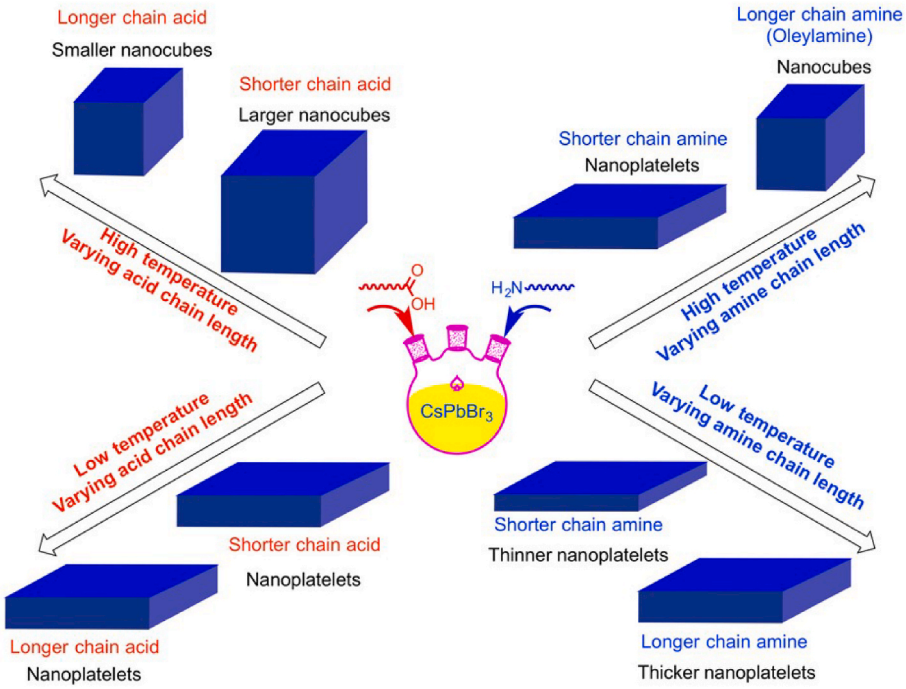

Fig. 3. Summary of the shape and size dependence on the chain length of carboxylic acids and amines. Reproduced with permission from Ref. [44]. Copyright 2016, American Chemical Society.

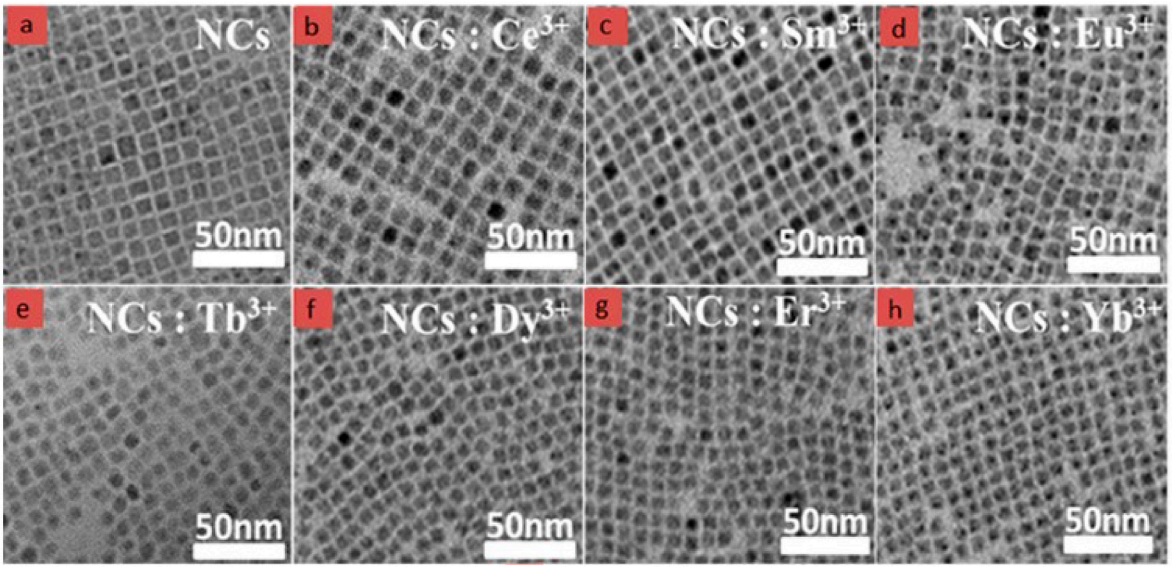

Fig. 4. (a–h) Transmission electron microscopy (TEM) images of $CsPbCl_3$ and different lanthanide (Ce^{3+}, Sm^{3+}, Eu^{3+}, Tb^{3+}, Dy^{3+}, Er^{3+}, Yb^{3+}) $CsPbCl_3$ NCs. Reproduced with permission from Ref. [46]. Copyright @ 2017, American Chemical Society.

Table 1
Different lanthanide-based MHP NCs along with synthesis process and luminescence peak.

Materials	Dopant	Synthesis technique	Luminescence Peak (nm)	Ref
$CsPbCl_3$	Ce^{3+}, Sm^{3+}, Eu^{3+}, Tb^{3+}, Er^{3+}, Yb^{3+}	Modified hot injection	420–980	[45]
$Cs_2NaInCl_6$	Tb^{3+}, Bi^{3+}	Modified hot injection	988	[50]
$CsPbCl_3$	Yb^{3+} Yb^{3+}/Er^3	Modified hot injection	986 1533	[47]
CsPbBr3	Ce^{3+}	Hot injection	510	[51]
$CsPbCl_{3-x}Br_x$	Eu^{3+}	Modified hot injection	590–700	[52]
$CsPbBrCl_2$	Yb^{3+}, Ce^{3+}, Sm^{3+}, Eu^{3+}	Hot injection		[53]
$CsPbCl_3$	Yb^{3+}	Hot injection	1000	
$CsPbBr_3$	Eu^{3+}	Hot injection	498	[54]
$CsPb(Cl_{1-x}Br_x)_3$	Yb^{3+}	Hot injection	984	[55]
$CsPbCl_3$	Sm^{3+}	Modified Hot injection	410	[56]
$CsPbI_3$	La^{3+}	Hot injection	690	[57]
$CsPbBr_3$	Nd^{3+}	Hot injection	478	[58]
$Cs_2AgInCl_6$	Yb^{3+}	Hot injection	994	[59]
$Cs_2AgInCl_6$	Ce^{3+}	Hot injection	589	[60]
$CsPbBr_3$	Nd^{3+}	LARP	459	[61]
$Cs_2AgInCl_6$	Bi^{3+}-Yb^{3+}	LARP	994	[62]
$Cs_3Bi_2Br_9$	Sm^{3+}	LARP	445	[63]
$CsPbBr_3$	Yb^{3+}, Ce^{3+}, Sm^{3+}, Eu^{3+} Nd^{3+}, Gd^{3+}, Tb^{3+}, Ho^{3+}, Er^{3+}, Lu^{3+}	Thin film synthesis		[64]
$MAPbI_3$	Eu^{2+}, Sm^{3+}, Tb^{3+}	Thin film synthesis		[65]

shown in Fig. 7, all lanthanide-based DMHP NCs have similar XRD patterns, matching well with simulated XRD patterns. The TEM images in Fig. 7(b-h) show no significant changes in the images with different lanthanide ions.

2.2. Ligand-assisted reprecipitation (LARP)

Supersaturated crystallization is a simple process that involves dissolving the chosen ions in a solvent to reach an equilibrium concentration. Subsequently, the solution reaches a nonequilibrium state of supersaturation. This supersaturation can be achieved under different conditions, such as an appropriate temperature, solvent evaporation, and addition of a miscible co-solvent. When crystallization is performed in the presence of ligands, it is known as LARP. The synthesis of MHP NCs via the LARP method involves dissolving the precursors in a polar solvent, such as dimethylformamide or dimethylsulfoxide (DMSO), and mixing the solution into a nonpolar solvent, such as hexane or toluene, in the presence of a ligand. A schematic representation of LARP is shown in Fig. 2., Xie et al. reported the synthesis of Nd^{3+}-doped $CsPbBr_3$ NCs by LARP at room temperature [61]. In this technique, the precursors $NdBr_3$, $PdBr_2$, and CsBr were dissolved in DMF, OA, and OLA, respectively, and the solution was added to toluene to form Nd^{3+}-doped $CsPbBr_3$ NCs. The cubic-phased Nd^{3+}-doped $CsPbBr_3$ NCs with a uniform particle size distribution are shown in Fig. 8. With different doping of Nd^{3+} in the $CsPbBr_3$ NCs, no significant change was observed in the TEM images. Furthermore, Pan et al. reported Sm^{3+} doping of $Cs_3Bi_2Br_9$ MHPs by LARP.

The precursor solution was dropped into the above europium solution and vigorously stirred at 90 °C [63]. Sm^{3+}-doped NCs exhibited spherical and monodispersed morphologies. Ding et al. synthesized Eu^{3+}-doped $Cs_3Bi_2Br_9$ NCs by LARP. The precursors CsBr and $BiBr_3$ were

Table 2
Different lanthanide doping in $CsPbCl_3$ NCs along with properties. Reproduced with permission from Ref. [46]. Copyright 2017, American Chemical Society.

	$CsPbCl_3$	Ln^{3+} doped $CsPbCl_3$ NCs						
Dopant ions	NA	Ce^{3+}	Sm^{3+}	Er^{3+}	Tb^{3+}	Dy^{3+}	Er^{3+}	Yb^{3+}
Radius of dopant (Å)	NA	1.034	0.964	0.950	0.923	0.903	0.881	0.858
Lattice constant (101) (Å)	3.96	3.94	3.93	3.92	3.90	3.89	3.88	3.87
Bandgap (eV)	2.87	2.91	2.94	2.98	3.03	3.05	3.08	3.10
Doping concentration	NA	7.2	7.3	7.9	7.6	7.4	7.8	9.1
PLQY	3.8	24.3	14.1	27.2	31.2	27.6	15.1	142.7

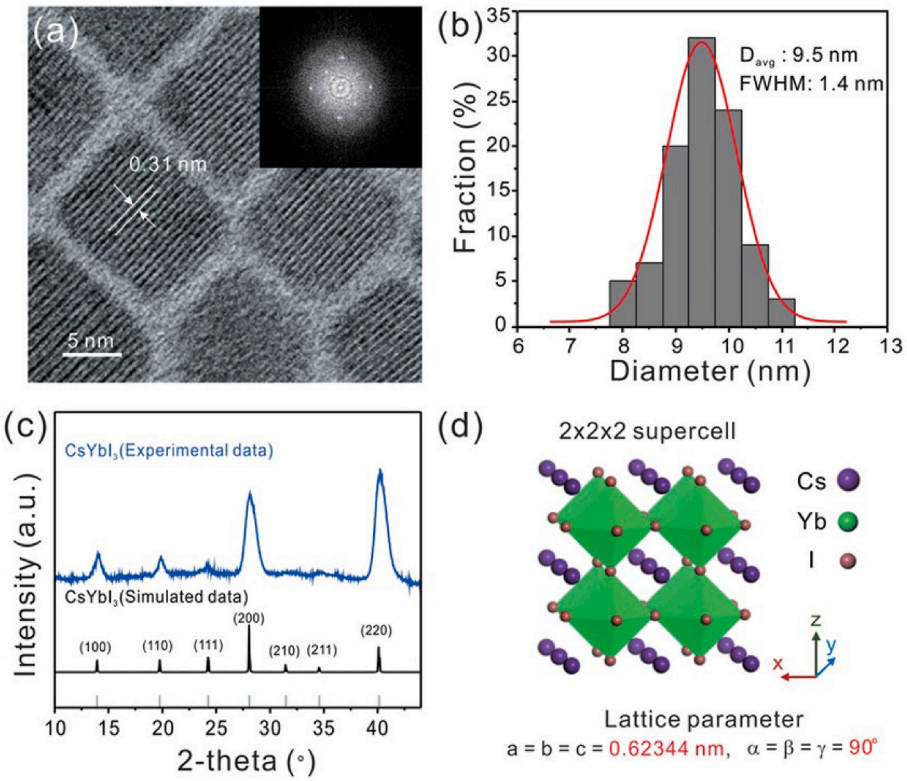

Fig. 5. (a–b) High resolution TEM image of $CsYbI_3$ NCs along with particle size distribution (c–d) X-Ray diffraction (XRD) pattern of $CsYbI_3$ NCs along with unit cell structure. Reproduced with permission from Ref. [38]. Copyright 2019, American Chemical Society.

dissolved in OLA, OA, and DMSO to form a homogeneous precursor solution. Additionally, different amounts of $EuBr_3$ wre dissolved in OA, and the ethanol solution was heated at 90 °C for 2 h. The time taken to form Eu^{3+}-doped $Cs_3Bi_2Br_9$ NCs was 10 min [66]. The Eu^{3+}-doped $Cs_3Bi_2Br_9$ NCs were formed with high crystallinity and uniform spherical shape. A list of lanthanide-based MHP NCs, which are synthesized using the LARP technique, is presented in Table 1.

2.3. Thin film synthesis

Over the last few decades, MHPs have been rapidly developed as optoelectronic materials for solar cell applications. Using the thin films of these compounds, solar cells have achieved excellent power conversion efficiencies (PCEs). Thin-film synthesis is useful for direct film fabrication in various device applications, including solar cells, LEDs, and photodetectors [67]. Thin films have been fabricated using solution-based techniques because of their simplicity and low cost. Generally, solution synthesis methods can be divided into one- or two-step processes. In one-step synthesis, all metal precursors are mixed in an organic solvent to form a homogeneous solution, which is then directly spin-coated onto a substrate and dried at a suitable temperature to obtain a perovskite thin film. In the two-step process, the first precursor solution is deposited on a substrate via spin coating and dried on a hot plate. The second precursor is coated onto the first precursor film via spin coating. The coated film is then heated on a hot plate to obtain a thin perovskite film. This procedure is repeated several times to obtain uniform perovskite thin films. MHPs and lanthanide-doped MHP thin films have been reported for solar cell applications. Recently, lanthanide-doped $CsPbBr_3$ films were synthesized using a two-step approach. Incorporating Ln^{3+} ions into perovskite films improves film uniformity and crystallinity and enlarges grain size, which significantly increases the performance of the solar cell devices as the recombination of charge carriers is prevented by the doping of Ln^{3+} ions [68]. Lanthanide (Sm^{3+}, Tb^{3+})-doped $MAPbI_3$ perovskite films were fabricated using a one-step process. The perovskite precursor solution containing lanthanide, lead, and organic ions is generally spin-coated at 100 rpm for 5 s and then at 2000 rpm for 60 s; it is then dried for 60 s obtain a thin film [65]. Lanthanide ions are introduced into the perovskite layer to improve its carrier diffusion and mobility.

3. Stability of MHP NCs

The stability of MHPs is a major limitation for their use in device applications. The stability of MHPs can be improved by many different approaches such as surface passivation, size reduction, and modification of the internal structure, including the partial replacement of A or B sites. The stability of MHPs can be significantly improved by using different organic passivating agents. To this end, organic passivating surfactants such as phenylethylammonium chlorine, phenylenediammonium, and p-phenylenediammonium iodide have been extensively studied [69]. The doping of metal ions in the B site affects the Goldsmith tolerance factor "t" and octahedral factor "μ," which determine the structure of ABX_3 NCs. As discussed before, cubic-phased ABX_3 is formed when "t" lies between 0.9 and 1. Larger A values increase the "t" value to near unity and enhance stability. The stability of the MHPs significantly depends on the size of $[BX_6]^{4-}$, and Cs^+ is the largest cation that can be used in perovskite structures. Lanthanide doping in the ABX_3 NCs provide a few advantages, such as a) enhancing the "t" value by reducing the size of $[BX_6]^{4-}$, as most Ln^{3+} ions are smaller than Pb^{2+} ions; b) reducing the usage of toxic elements; and c) reducing the grain boundary and trap states [70]. Xia et al. demonstrated enhanced stability of $CsPbI_3$ by La^{3+} doping [71]. The partial substitution of Pb^{2+} ions (119 p.m.) with smaller La^{3+} (103 p.m.) ions enhances the formation energy of $CsPbI_3$. Further, the strong interaction between the La^{3+} and I^- ions in the octahedra reduce the trap states. La^{3+}-doped $CsPbI_3$ NCs also demonstrate superior carrier transport by improving the energy band for narrowed hole injection. The stability of La^{3+}-doped $CsPbI_3$ NCs is shown in Fig. 9. Furthermore, Nd^{3+} doping of $CsPbCl_3$ NCs results

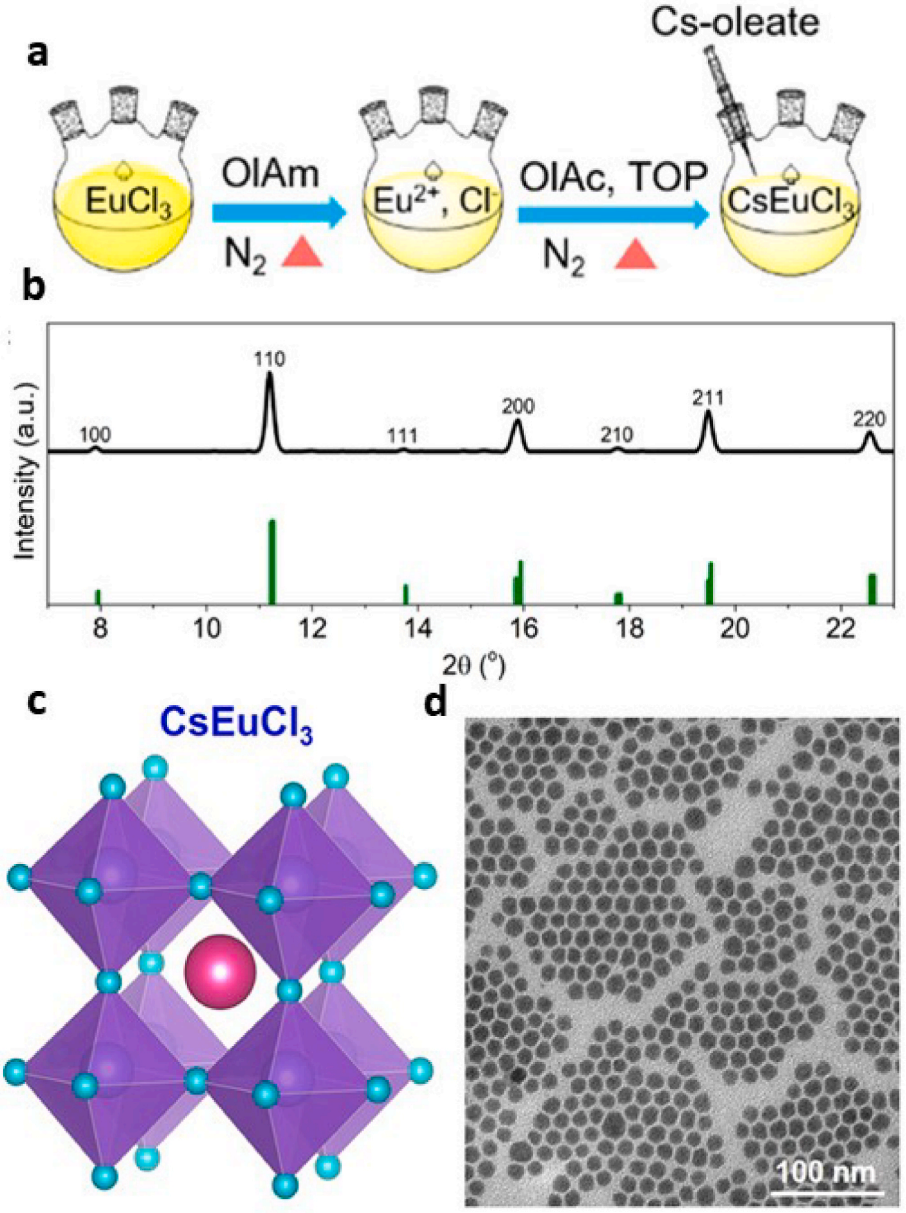

Fig. 6. (a) Schematic of $CsEuCl_3$ NCs synthesis, (b–c) XRD and unit cell structure of (d) TEM images of $CsEuCl_3$ NCs. Reproduced with permission from Ref. [37]. Copyright 2020, American Chemical Society.

in enhanced stability [72]. Partial substitution of Pb^{2+} (119 p.m.) with Nd^{3+} (98 p.m.) results in a decrease in the number of octahedral sites, which leads to an increase in the tolerance factor. Thus, Nd^{3+} doping enhances the stability of the $CsPbBr_3$ NCs. The Nd^{3+}-doped $CsPbBr_3$ NCs exhibit better thermal stability than pristine $CsPbBr_3$ NCs. Nd^{3+}-doped $CsPbBr_3$ NCs retained 90% of the initial PL intensity, whereas pristine $CsPbBr_3$ NCs retain 60% of the initial P intensity. Similarly, Xu et al. demonstrated enhanced stability of $CsPbCl_3$ with Yb^{3+} doping [73].

4. Optical properties

In MHPs, when a photon with ample energy excites a material, electrons (e) are promoted from the valence band to the conductance band. As a result, the creation of electrons and holes (h) and the radiative recombination of the e–h pair create emission. This emission mechanism is known as the interband emission of MHPs [74–76]. Moreover, the Coulombic attraction between electrons and holes creates a quasiparticle called an exciton. The recombination of e–h and excitons generates excitonic emission. The excitonic energy is generally equal to the bandgap of the MHPs. Self-trapped excitons are generated when e–h pairs are strongly coupled to the lattice. Metal halide perovskite NCs ($CsPbX_3$) exhibit unique optical properties such as defect tolerance, narrow bandwidth, quantum confinement, high PLQY, and tunable emission [1,77–79]. Interestingly, the emission of $CsPbX_3$ NCs can be tuned from 400 to 700 nm, as shown in Fig. 10 [6]. Similarly, $CsPbX_3$ NCs exhibit absorption in the UV to visible region (300–700 nm). The MHP NCs showed narrow emission peaks with a full width at half maximum (HWHM) of 11–37 nm. Therefore, the MHP NCs exhibit very high color purity, which is essential for display applications. Similarly, $FAPbX_3$ NCs (X = Cl, Br, I and FA = Formamidinium) exhibited color gamut in the range of 400 to 750 nm as shown in Fig. 10 [80]. However, the FWHMs were in the range of 20-44 nm, which is relatively higher compared to $CsPbX_3$ NCs. The PL properties depends on the thickness of the nanoplates as shown in Fig. 10c.

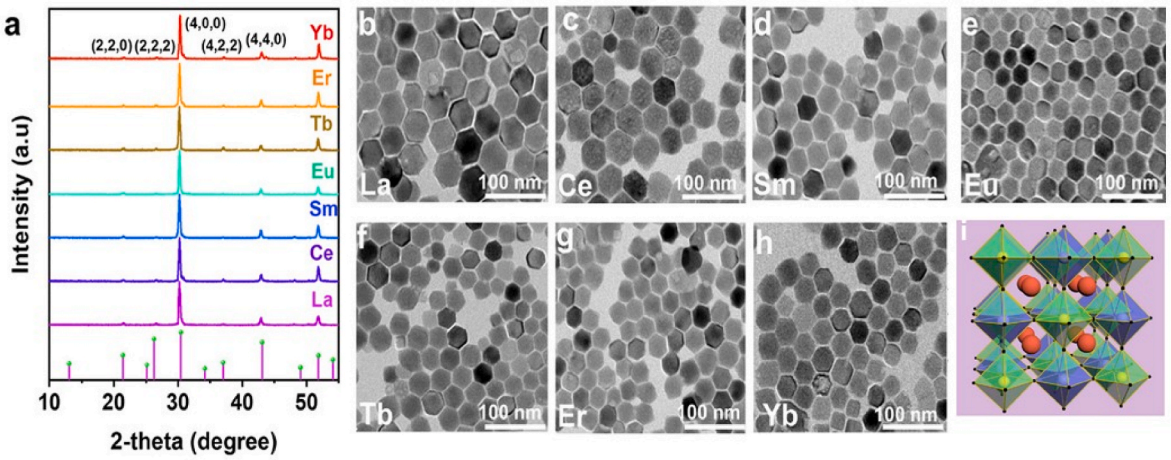

Fig. 7. (a) XRD of $Cs_2NaLnBr_6$ NCs, (b–h) TEM images of $Cs_2NaLaBr_6$, $Cs_2NaCeBr_6$, $Cs_2NaSmBr_6$. $Cs_2NaTbBr_6$, $Cs_2NaErBr_6$, and $Cs_2NaYbBr_6$, respectively. (i) Unit cell structure of $Cs_2NaLnBr_6$ NCs. Reproduced with permission from Ref. [39]. Copyright 2023, Wiley-VCH.

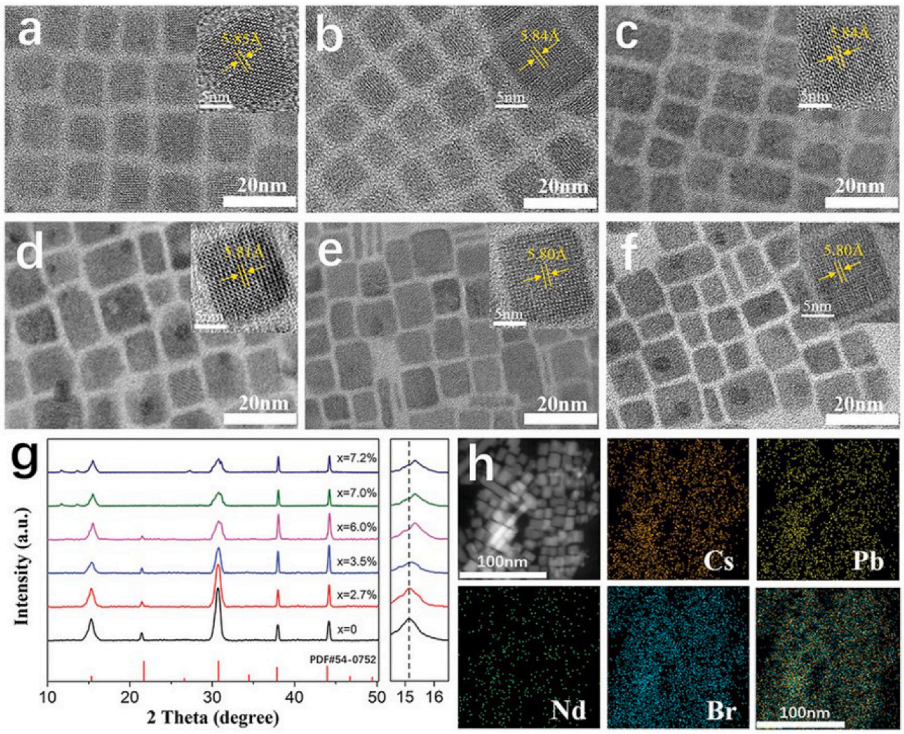

Fig. 8. (a–f) TEM images of Nd^{3+}-doped $CsPbBr_3$ NCs with different doping ratios of Nd^{3+}. (g) XRD pattern of different Nd^{3+}-doped $CsPbBr_3$ NCs. (h) Elemental mapping of Nd^{3+}-doped $CsPbBr_3$ NCs. Reproduced with permission from Ref. [61]. Copyright 2020, Wiley-VCH.

4.1. Lanthanide-based MHPs

Lanthanide ions ($Ln^{3+/2+}$) exhibit unique optical properties because of their *4f-4f* transitions. Moreover, the *4f* orbitals are shielded from the outer environment by the outer $5s^2$ and $5p^6$ orbitals. Therefore, lanthanides possess very interesting optical properties such as large stokes/anti-stokes shifts, narrow emission band, high luminescence, long lifetimes (μs to ms), and excellent photostability [81–84]. These properties are attractive for applications in solid-state lighting, sensing, bioimaging, therapy, photovoltaic, etc [85,86]. Additionally, dipole-allowed interconfigurational $4f^n$-$4f^{n-1}$-5d transitions have been observed in Ln^{2+} ions such as Eu^{2+}, Sm^{2+}, Yb^{2+}, Tm^{2+} and in Ln^{3+} ions such as Ce^{3+} and Pr^{3+}. Materials that possess $4f^n$-$4f^{n-1}$-5d transitions show large molar absorptivities and higher PLQY owing to their partially allowed Laporte's selection rule. Additionally, the full-widths at half-maximum.

(FWHM) of the emission bands arising from $4f^n$-$4f^{n-1}$-5*d* transitions are broader than those of the *4f-4f* transitions.The energy of the $4f^n$-$4f^{n-1}$-5*d* transitions varies with the outer environment, such as ligand nature, charge polarizability, and coordination number, according to crystal field theory. The optical properties of lanthanide-based materials have been extensively studied in the upconverting fluoride host lattices such as $NaYF_4$, LaF_3, and SrF_2. Moreover, the substitution of Ln^{3+} ions (Ce^{3+}, Eu^{3+}, Nd^{3+}, Yb^{3+}, Sm^{3+}, and Tb^{3+}) in MHPs may influence their optical properties because of the differences in the chemical nature of Pb-X and Ln-X. Recently, several lanthanide-doped $CsPbX_3$ NCs have been reported [2,87]. For example, Pan et al. have synthesized a series of Ln^{3+} (Ce^{3+}, Sm^{3+}, Eu^{3+}, Tb^{3+}, Dy^{3+}, Er^{3+}, Yb^{3+}) doping in the $CsPbCl_3$ NCs

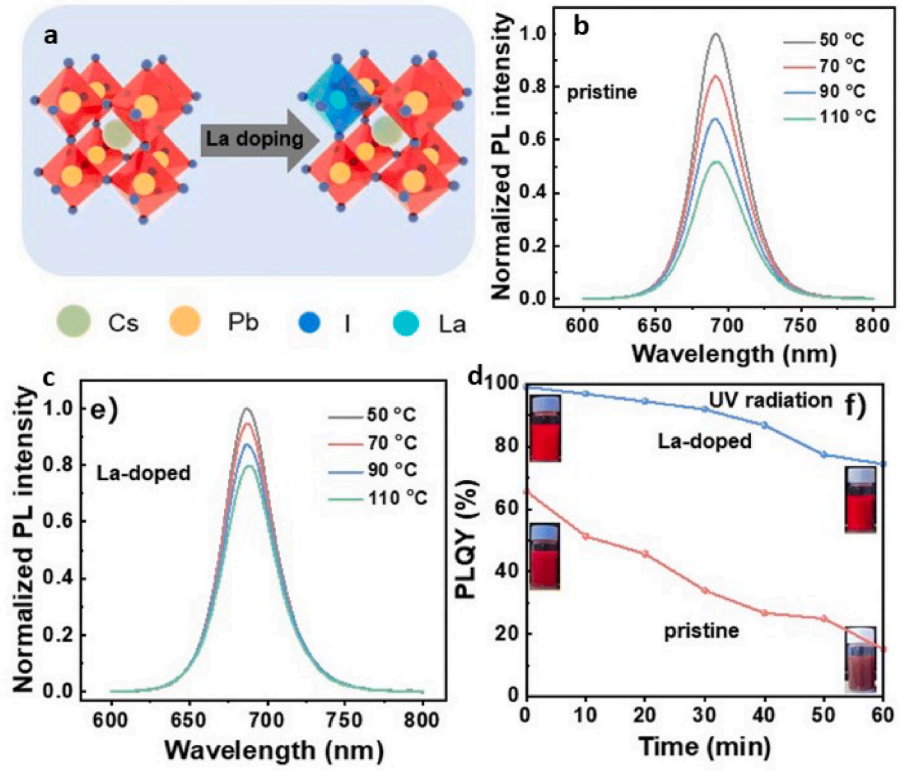

Fig. 9. (a) Schematic of La^{3+} doping in the unit cell of $CsPbI_3$ NCs. (b–c) Temperature-dependent PL spectra of $CsPbI_3$ NCs and La^{3+} doped $CsPbI_3$ NCs. (b) Photostability with respect to PLQY. Reproduced with permission from Ref. [71]. Copyright 2023, Royal Chemical Society.

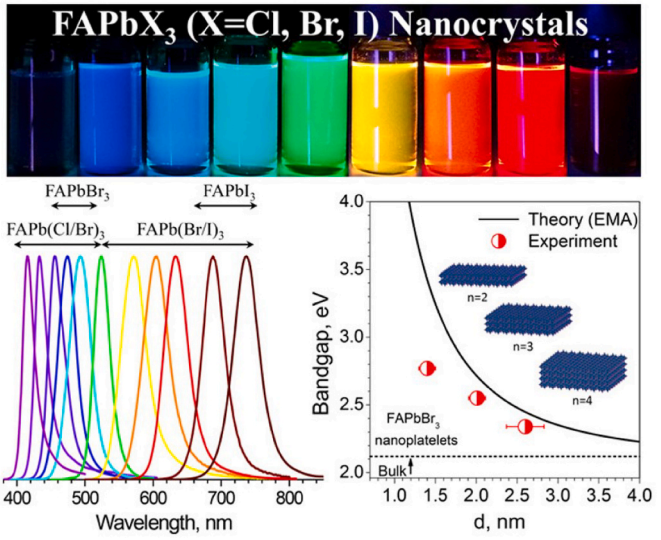

Fig. 10. MHP $FAPbX_3$ NCs (X = Cl, Br, I) exhibit size- and composition-tunable bandgap energies covering the entire visible spectral region with narrow and bright emissions: (a) $FAPbX_3$ NCs (X = Cl, Br, I) solutions in toluene under UV lamp (λ_{ex} = 365 nm); (b) representative PL spectra (λ_{ex} = 365 nm for all $FAPbX_3$ NCs (X = Cl, Br, I) samples); (c) Theoretical vs experimental bandgap of $FAPbX_3$ NCs (X = Cl, Br, I) as a function of thickness. Reproduced with permission from Ref. [80]. Copyright 2017, American Chemical Society.

via modified hot injection method as we discussed above [46]. Interestingly, based on Ln^{3+} doping, the emission color changes from the UV to the NIR region, as shown in Fig. 11. Moreover, as shown in Fig. 12a, absorption of the $CsPbCl_3$ NCs shifts to a higher energy with increasing atomic number of the lanthanide dopants, which is due to the increase in the bandgap of the host MHP upon decrease in the size of the lanthanide ions. Upon illumination with 365-nm light, the undoped $CsPbCl_3$ NCs exhibit a narrow characteristic emission band at 410 nm. In the case of the Ln^{3+}-doped $CsPbCl_3$ NCs, the host materials efficiently transfer energy to the Ln^{3+} ions, which emit energy in the visible to NIR region (Fig. 12b). The optical properties of the $CsPbCl_3$ NCs and Ln^{3+}-doped $CsPbCl_3$ NCs are summarized in Table 2. Change et al. also demonstrated the sensitization of Sm^{3+} and Yb^{3+} emissions via $CsPbCl_3$ host materials. Recently, Xia et al. has reported a La^{3+}-doped $CsPbI_3$ NCs with 99.3% PLQY.

Moreover, the use of Eu^{2+} and Yb^{2+} instead of Pb^{2+} provides an excellent replacement for LHPs. Moon et al. recently reported $CsYbI_3$ NCs with a bandage emission at 664 nm [38]. Upon 450-nm excitation, $CsYbI_3$ NCs emit a strong emission peak 671 nm with a FWHM of 47 nm. The corresponding absorption and PL spectra are shown in Fig. 13a. Further, the excitation-dependent PL spectra are shown in Fig. 13b. The $CsYbI_3$ NCs exhibit excitation-independent PL behavior when excited between 350 and 550 nm, and the temperature-dependent PL shows that $CsYbI_3$ is more thermally stable than $CsPbI_3$. The superior thermal PL stability of $CsYbI_3$ is due to the Yb^{2+} induced charge-compensating defects serving as radiative recombination centers. $CsYbI_3$ NCs also retained 88% of their original PL intensity upon exposure to ambient conditions for 15 days. Furthermore, Haung et al. developed a blue emitting $CsEuCl_3$ NC, which showed strong excitonic absorption bands in the range 300–400 nm, with a maximum at 350 nm. The optical bandgap was 3.07 eV, which was calculated from the Tauc plot. The absorption and Tauc plots are presented in Fig. 13c. The $CsEuCl_3$ NC solution exhibited a bright blue emission at 435 nm with a narrow FWHM of 19 nm. This blue emission is attributed to the dipole allowed $4f^6 5\,d^1$-$4f^7$ transition. The PL excitation (PLE) spectra were measured by monitoring the emission peak at 435 nm, which was similar to the absorption peak of $CsEuCl_3$. The PL and PLE of $CsEuCl_3$ NCs are shown in Fig. 13d. However, the PLQY of the NC solution was approximately 2% at room temperature, which increased to ~6% after passivation with

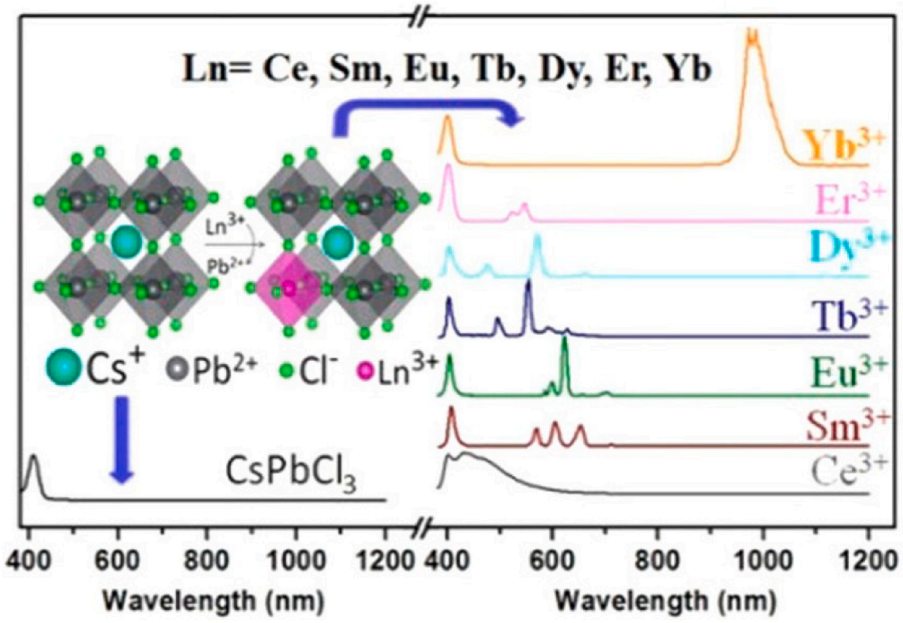

Fig. 11. Lanthanide doping in the $CsPbCl_3$ NCs along with PL spectra and unit cell structure. Reproduced with permission from Ref. [46]. Copyright 2017, American Chemical Society.

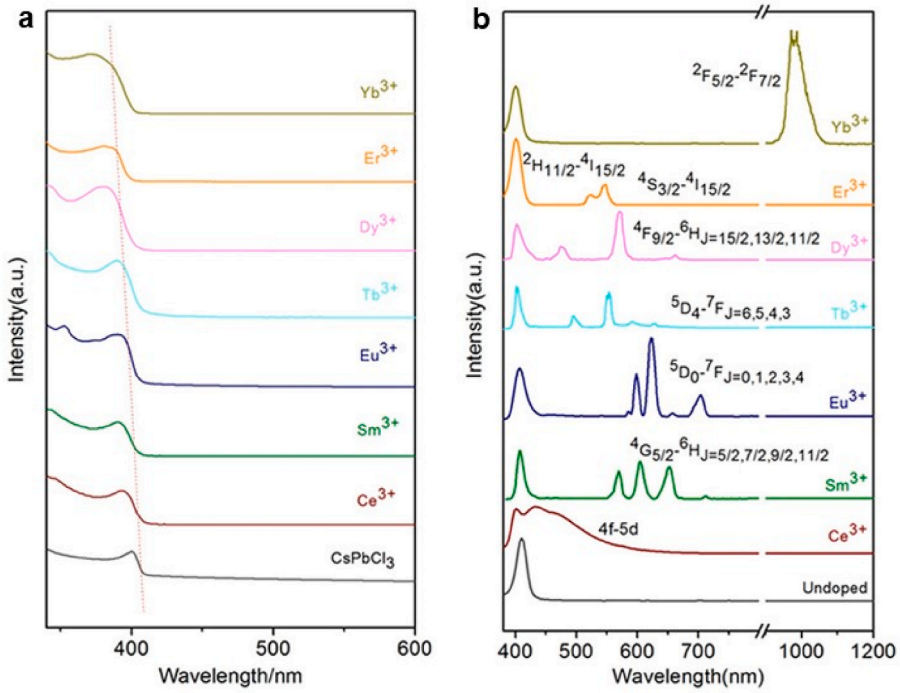

Fig. 12. Optical properties of different lanthanide-based $CsPbCl_3$ NCs: a) absorbance spectra, b) luminescence spectra. Reproduced with permission from Ref. [46]. Copyright 2017, American Chemical Society.

1-butyl-1-methylpyridinium chloride. The time resolved photoluminescence (TRPL) decay curves of the $CsEuCl_3$ NCs was fitted to a biexponential decay with a component of 4.4 ns and another with 30.9 ns.

Among the lead-free MHP NCs, DMHPs are prominent materials in the perovskite family because of their unique dimensionality and tunable bandgap, which are achieved by alloying with isovalent doping at the B site. Recently, Song et al. synthesized a series of lanthanide-based DMHPs [39]. For instance, Cs_2NaLnX_6 (Ln = La, Ce, Sm, Eu, Tb, Er, Yb, and X = Cl, Br, and I) NCs exhibit interesting optical properties. For the $Cs_2NaLnCl_6$ and $Cs_2NaLnBr_6$ NCs, a band-edge absorption peak was observed at 307 nm; however, an extra peak was observed at 363 nm for the Cs_2NaLnI_6 NCs, as shown in Fig. 14(a-c). Under 365-nm excitation, all $Cs_2NaLnCl_6$ NCs exhibited a broad emission band at 438 nm with an FWHM of 78 nm. Similarly, $Cs_2NaLnBr_6$ and Cs_2NaLnI_6 NCs exhibited broad peaks at 440 and 444 nm, respectively. A broad emission peak was observed owing to self-trapped excitons (STEs). Moreover, the broad emission does not change with different ligand attachments, confirming the formation of STEs (Fig. 14). For further confirmation of the STEs, the emission was demonstrated via

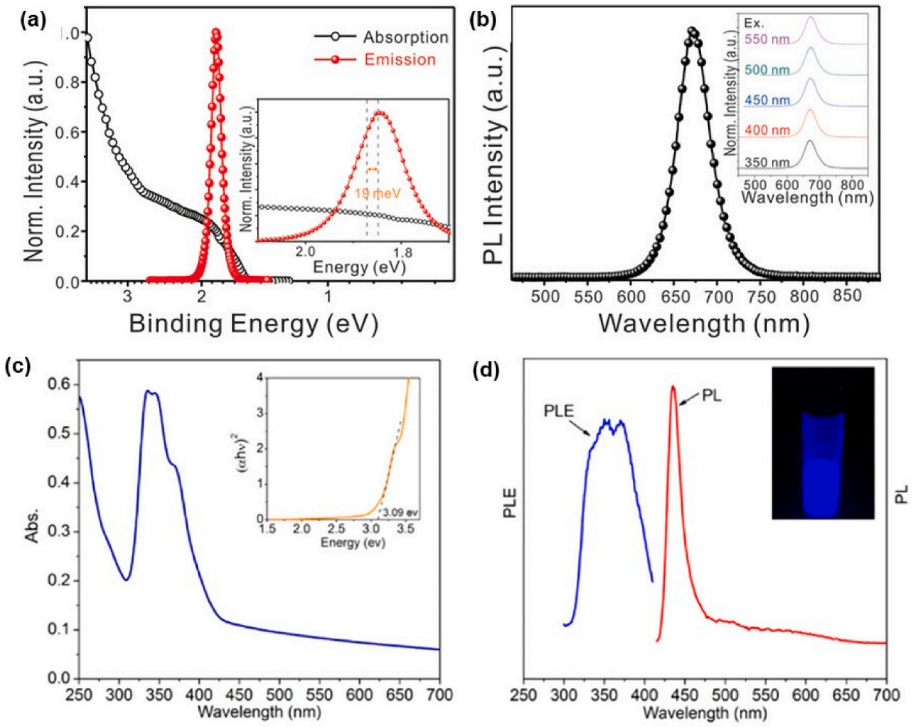

Fig. 13. a) Absorption and PL spectra of $CsYbI_3$ NCs in toluene. b) PL spectra of $CsYbI_3$ NCs upon 450 nm excitation. Inset shows the excitation dependent PL in the range 350 to 550 nm. c) Absorption and Tauc plot (inset) of $CsEuCl_3$ NCs. b) PL (red) and PLE spectra of $CsEuCl_3$ NCs Reproduced with permission from Ref. [38]. Copyright 2019, American Chemical Society. (For interpretation of the references to color in this figure legend, the reader is referred to the Web version of this article.)

temperature-dependent FWHM calculations (Fig. 14e) and ultrafast spectrum tests, as shown in Fig. 14f. These analyses confirm the strong electron–phonon coupling, which is essential for STE emissions. Moreover, upon excitation at 365 nm, the Cs_2NaEuX_6 and Cs_2NaEuX_6 NCs showed the characteristic peaks of Tb^{3+} and Eu^{3+} at 545 and 617 nm, respectively (Fig. 14(a-c)). Evidently, other lanthanide-based NCs did not show characteristic emissions owing to the small bandgaps assisted by Cs_2NaLnX_6.

4.2. Quantum cutting luminescenec

Quantum-cutting luminescence (QCL) or down-conversion is the conversion of one high-energy photon into two or more lower-energy photons [88]. The PLQY of QCL is greater than 100%, and QCL was first reported for YF_3:Yb^{3+} materials For the first time, Zhou et al. demonstrated QCL in Ce^{3+} and Yb^{3+} co-doped $CsPbCl_3$ NCs with a PLQY of 146% [89]. Milstein et al. demonstrated QCL of Yb^{3+}-doped $CsPbX_3$ (X = Cl, Cl/Br) at 990 nm with a PLQY of 170% [90]. Subsequently, Li et al. proposed a QCL mechanism, as shown in Fig. 15b [91]. Their calculation did not find any energy level formed in the middle of the $CsPbCl_3$ bandgap, which forbids a stepwise energy transfer mechanism from the MHP NCs to the Yb^{3+} ions. They indicated that "right-angle" Yb^{3+}-V_{Pb} -Yb^{3+} couple is possibly formed in the Yb^{3+}-doped $CsPbCl_3$. The "right angle" couple associated with "right angle" Pb atom with trapped excited states localizes the photogenerated electrons and acts as the energy donor in the quantum cutting process.

5. Application of lanthanide-based MHP NCs

MHP NCs continue to gain importance for white light-emitting diodes (WLEDs), photovoltaics, and other optoelectronic applications. In recent years, lanthanide-based MHP NCs have been investigated to increase the efficiency and stability of photovoltaics. In addition to the use of WLEDs and photovoltaics, lanthanide-based MHP NCs are employed in many emerging fields, such as optical temperature sensing, NIR imaging, photodetectors, and optical security encoding. In this review, we focus on the solid-state lighting of lanthanide-based MHP NCs.

5.1. White light-emitting diodes

MHPs NCs possess near-unity PLQY with a very high absorption coefficient, which allows for many interesting optoelectronic applications. Color-converted WLEDs are an interesting application [24,92,93]. The WLEDs are very important for solid-state lighting (SSL). The main commercially available WLEDs are based on blue-emitting InGaN LED chips coated with downshifting $Y_3Al_5O_{12}$:Ce^{3+} (YAG:Ce^{3+}) phosphors [94]. However, existing phosphor-coated WLEDs suffer from a poor color rendering index (CRI). Recently, lanthanide-based MHPs NCs have been widely explored for use in color converted LEDs. Yuan et al. synthesized 20% Yb^{3+}-doped $CsPbI_3$ with 66% PLQY and fabricated WLEDs by integrating a GaN blue LED chip and YAG:Ce^{3+} phosphor [95]. The fabricated WLEDs exhibited a high CRI of 85.4, low color conversion temperature (CCT) of 3524 K, and luminescence efficiency of 57 lmW^{-1}. Pan et al. constructed WLEDs with different lanthanide-co-doped MHPs NCs. Pan et al. fabricated WLEDs with $CsPbCl_3$ and $CsPbCl_xBr_{3-x}$ MHP NCs co-doped with different metal ion pairs, such as Ce^{3+}/Mn^{2+}, Ce^{3+}/Eu^{3+}, Ce^{3+}/Sm^{3+}, Bi^{3+}/Eu^{3+}, and Bi^{3+}/Sm^{3+} [96]. The performance of WLEDs is shown in Fig. 16. The schematics of WLED frabrication is shown in Fig. 16a. Fig. 16b exhibited the PL spectra of 2.7% Ce^{3+}/9.1% Mn^{2+}-codoped $CsPbClxBr_{3-x}$ NCs. The CIE coordination of of the WLED from 2.7% Ce^{3+}/9.1% Mn^{2+} is shown in Fig. 16c. PL images of 2.7% Ce^{3+}/9.1% Mn^{2+}-codoped $CsPbCl_xBr_{3-x}$ NCs and WLEDs is shown in insets of Fig. 16d. Further, Fig. 16e exhibited the Pl spectra of WLED at difefrent time. Finally, Fig. 16f showed the normalized integrals of the emission peaks at 429, 460, and 592 nm for 2.7% Ce^{3+}/9.1% Mn^{2+}-codoped $CsPbCl_xBr_{3-x}$ NCs NC. The optimized WLED with Ce^{3+}/Mn^{2+}-co-doped $CsPbCl_{1.8}Br_{1.2}$ NCs exhibited a PLQY of 72 ± 3 and luminous efficacy (LE) of 51 lmW^{-1}. The color coordinates of the WLED were (0.33, 0.29). Moreover, the introduction of Ce^{3+} ions into the $CsPbCl_3$ NCs also enhanced the sensitivity of emission from other ions, such as Mn^{2+}, Eu^{3+}, and Sm^{3+}, to red emission. Luo et al. reported efficient exciton energy transfer from a perovskite host to Mn^{2+} via $^1G_4$ energy level of Tm^{3+} in Tm^{3+}/Mn^{2+}-co-doped

$CsPbBr_{2.2}Cl_{0.8}$ [97]. The optimized NCs produced single-component white light with CIE color coordinates of (0.34, 0.33) and a PLQY of

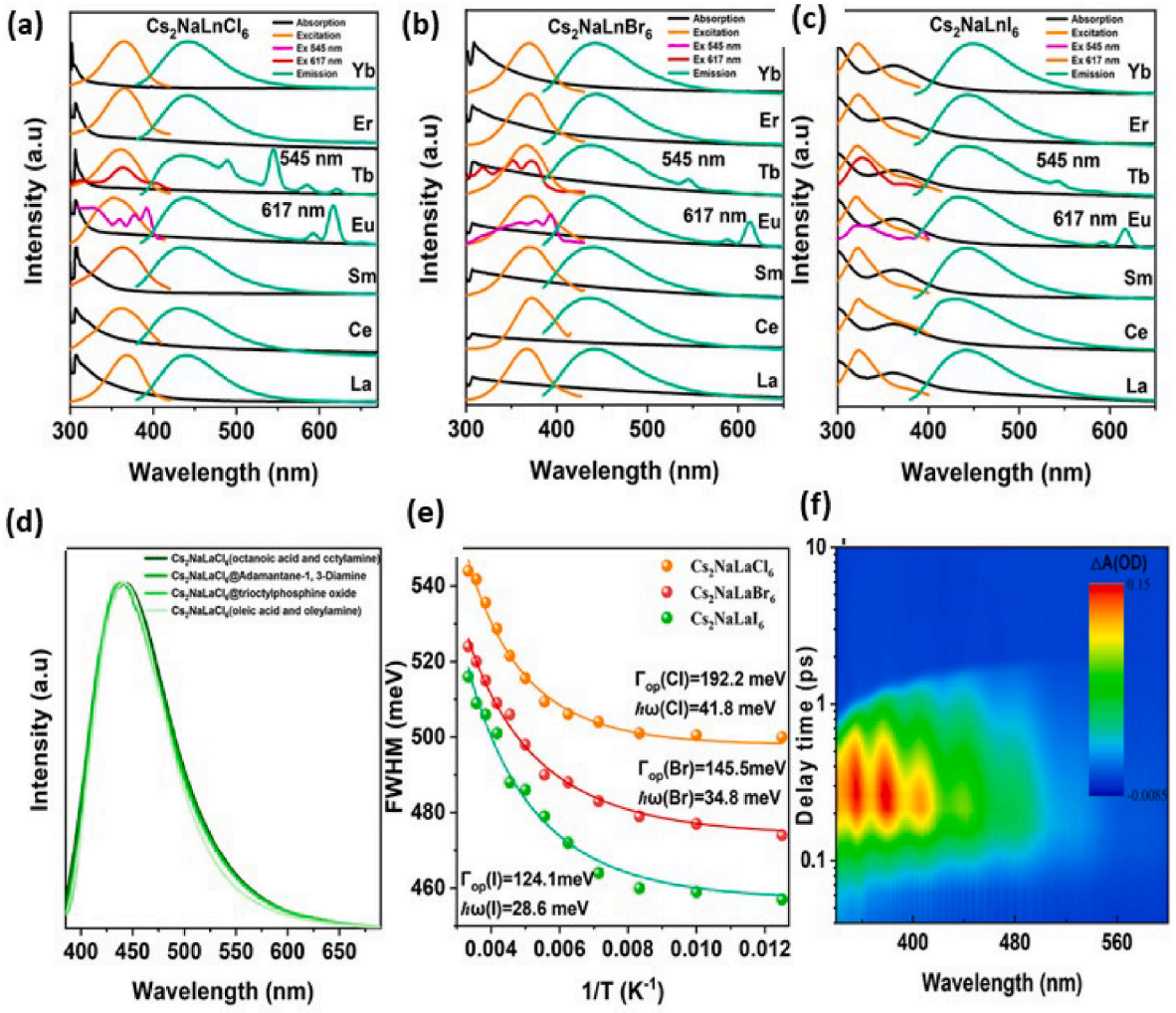

Fig. 14. Optical properties of Cs_2NaLnX_6 NCs. (a–c) Absorption, emission, and excitation spectra of $Cs_2NaLnCl_6$, $Cs_2NaLnBr_6$, and Cs_2NaLnI_6 NCs (λ_{ex} 365 nm, monitoring the wavelength of 438, 440, 444, 545, and 617 nm). d) The emission spectra of $Cs_2NaLaCl_6$ NCs with different ligands. e) Fitting results of the FWHM (meV) as a function of 1/T (K^{-1}). f) Contour plots of the fs-TA spectra of $Cs_2NaLaCl_6$ NCs upon excitation with a 320 nm fs-pulsed laser. Reproduced with permission from Ref. [39]. Copyright 2023, Wiley-VCH.

54%. Moreover, a WLED was fabricated on 365 nm LED chip, which exhibited standard white light emission with CIE of (0.33, 0.34) and color rendering index CRI) up to 91. Xiang and co-worker has synthesized Gd^{3+} doped $CsPbCl_3$ NCs in borosilicate glass (B_2O_3–SiO_2–ZnO) [98]. WLEDs were prepared by blending Gd^{3+}-doped $CsPbBr_2I$@glass and YAG:Ce^{3+} phosphors with blue LEDs. The optimized WLED device demonstrated a high LE of 90.09 lm/W with CIE chromaticity coordinates of (0.334, 0.3386). Moreover, the CCT and CRI were 5434 K and 81.4, respectively. Erol et al. constructed a WLED device with Eu^{3+}/Dy^{3+}-co-doped $CsPbBr_3$ NCs in glass on top of a 400-nm wavelength LED chip [99]. The fabricated WLED showed a CIE coordinates of (0.3349, 0.3986), CRI of 78, and CCT of 5436 K (see Fig. 16). Lee and co-worker has demonstrated a WLED via photon upconversion (UC) in $NaYF_4$:Yb^{3+},Tm^{3+}@$NaYF_4$/$CsPb(Br_{1-x}/I_x)_3$ composites [100]. The achieved white light spectral profile generated a CIE chromaticity coordinate of (0.318, 0.301), and CCT of 6361 K. Song and co-worker have generated a single component white light from Cs_2Na(Tb:Eu = 25:1)Cl_6 NCs upon 365 nm excitation, which is shown in Fig. 17a [39]. The white light emission showed a 500 h long stability under 365 nm excitation Fig. 17 (b). The fabricated WLED with Cs_2Na(Tb:Eu = 25:1)Cl_6 NCs demostrated an excellent WLED performance with CIE chromaticity coordinates of (0.334, 0.320), CRI of 91.2, and CCT of 5547K that match with the commercial standard. A summery of WLEDs based on lanthanide MHPs is presented in the Table 3(see Table 4).

5.2. Perovskite solar cell

MHP NCs based perovskite solar cells (PSCs) have attracted considerable attention owing to their superior properties. The unique properties of MHPs NCs such as high absorption coefficient in the visible region, long carrier diffusion length, tunable bandgap, and low-cost solution processing lead to outstanding photovoltaic performance of PSCs. PSCs have achieved a PCE of 25.5% by 2021 [103]. However, the stability and efficiency of PSCs are still hurdles to their commercialization as they cannot match commercial standards. To overcome the instability due to heat, moisture, and light and to improve the PCE, several efforts have been made, such as the use of Lewis base additives, metal ions, and halide ion doping. Among these, doping metal ions into MHP NCs can control the crystal growth and bandgap tuning and enhance the built-in electric fields, leading to a significant enhancement in the stability and PCE of PSCs. In this regard, lanthanide metal cations ($Ln^{3+/2+}$) possess a similar ionic radius and lattice constant to Pb^{2+}, which is ideally suitable for the B sites in the ABX_3 structure. $Ln^{3+/2+}$ ions with unique optoelectronic properties have been widely employed to eliminate deep defects and improve the film quality of superconductors and multiferroic materials. According to theoretical studies,

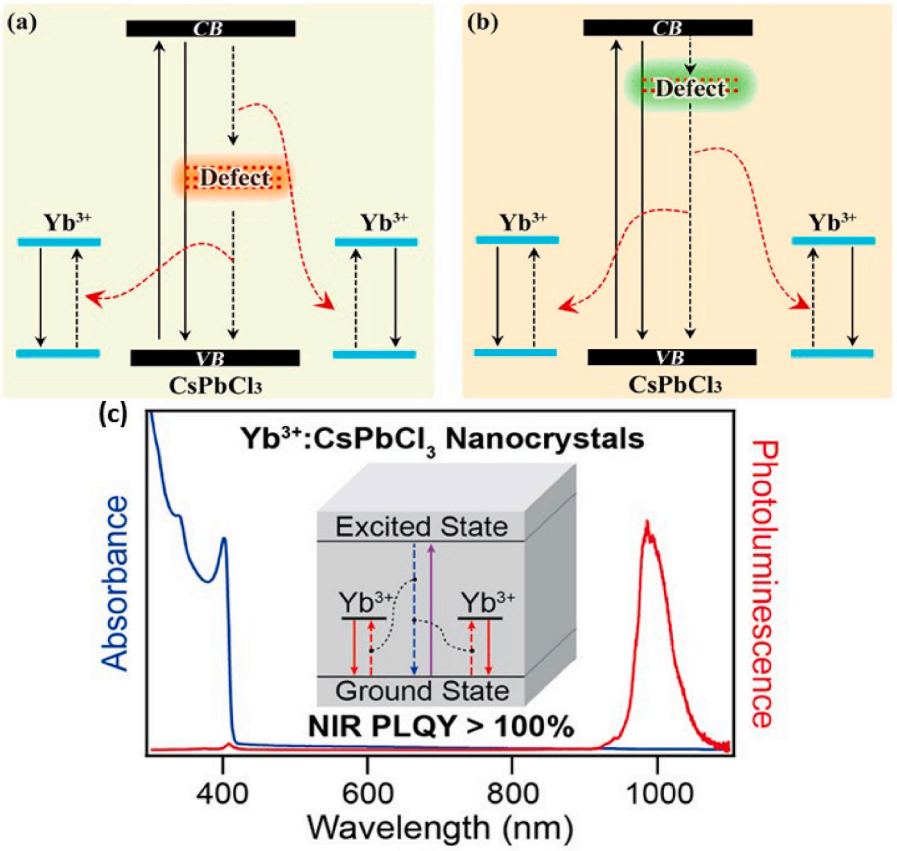

Fig. 15. a) Schematic of (a) stepwise energy transfer mechanism, (b) QCL mechanism of Yb^{3+} doped $CsPbCl_3$ NCs. Copyright 2019, American Chemical Society. (c) QCL of Yb^{3+} doped $CsPbCl_3$ NCs. Reproduced with permission from Refs. [90,91]. Copyright 2018, and 2019, American Chemical Society.

$Ln^{3+/2+}$ doping influences the electronic structure owing to its electronegativity, which can alter the work junction and valence band. Duan et al. demonstrated the incorporation of Ln^{3+} (La^{3+}, Ce^{3+}, Nd^{3+}, Sm^{3+}, Eu^{3+}, Gd^{3+}, Tb^{3+}, Ho^{3+}, Er^{3+}, Yb^{3+}, and Lu^{3+}) into the $CsPbBr_3$ films, and the performance of the PSC enhanced significantly, achieving an efficiency of 10.14% and ultrahigh open-circuit voltage of 1.594 V under one sun illumination [104]. Song et al. reported the incorporation of different Ln^{3+} ions such as Ce^{3+}, Eu^{3+}, Nd^{3+}, Sm^{3+}, and Yb^{3+} into the MHPs films to which enhance the grain size and crystallinitythat improves the stability and increasing the PCE values significantly [105]. Moreover, Ce^{3+}-doped $MAPbI_3$ showed the best PCE performance of 21.67% compared to 18.5% for the pristine PSC. PSC with Ce^{3+}-doped $MAPbI_3$ also exhibited long-term chemical and UV-irradiation stability. The high performance of the PSCs after Ce^{3+} doping originates from the special Ce^{3+}/Ce^{4+} redox pair and unique 4*f*-5*d* absorption. Table 4shows the perormance of PSCs using lanthanide based MHPs [104-108].

5.3. Optical temperature sensing

Lanthanide-based MHPs have been investigated for various applications. Over the last few years, temperature sensing using photoluminescence (PL) and PL lifetimes have been extensively studied in lanthanide-based NCs. Lanthanide-based MHPs have also attracted interest for noncontact thermometry applications. In lanthanides, the PL intensity varies owing to the variation in the electron population in the thermally coupled states. However, the extremely small energy gap between these thermally coupled states leads to overlapping emissions. Electron–phonon coupling influences the change in temperature, which leads to a change in the PL intensity.

leads to the overlapping of the emission. The electron-phonon coupling influence with change of temperature that leads to the change of PL intensity. Therefore, lanthanide-based luminescence intensity ratio (LIR) thermometry is based on the two thermally couple energy levels (TCLs) of lanthanide ions, which follow Boltzmann distribution and generates thermal equilibrium.

$$\mathrm{LIR} = \frac{I_2}{I_1} = \mathrm{B}\exp\left(\frac{\Delta E}{K_B T}\right)$$

where I_2 and I_1 represent the integrated emission intensities from the transition of upper and lower TCLs respectively, T is the absolute temperature (K), E is the activation energy, and K_B is the Boltzmann constant [109]. Additionally, the absolute sensitivity is defined as $S_{A=}\frac{\partial LIR}{\partial T}$, and the relative sensitivity is expressed as $S_R = |\frac{1}{LIR}\frac{\partial LIR}{\partial T}| \times 100\%$. Zhang et al. reported on temperature sensing using Tb^{3+}-doped $CsPbI_3$ MHP NCs. Tb^{3+}-doped $CsPbI_3$ MHP NCs exhibited luminescence at 544 (Tb^{3+}) and 677 ($CsPbI_3$) nm [110]. The LIR value was calculated in the range 80–480 K. The S_A and S_R values of the thermometer based on the Tb^{3+}-doped $CsPbI_3$ MHPs were 0.034 K^{-1}, and 1.78% K^{-1}, respectively. Yao et al. also demonstrated temperature sensing in the range of 80–298 K using Dy^{3+}-doped $CsPbBr_3$ NCs with a relative sensitivity of 2.39 K^{-1} at 298 K [111]. Recently, Zhao et al. demonstrated temperature sensing in the range of 303–573 K using Er^{3+}-doped $Cs_3Bi_2Cl_9$ DMHPs [112]. $Cs_3Bi_2Cl_9$:Er^{3+} MHPs exhibited photon upconversion luminescence upon irradiation with 1550-, 980-, and 808-nm laser. The corresponding absolute sensitivity and relative sensitivity were 1.40 K^{-1} (808-nm excitation), 1.38 K^{-1} (980 nm), 1.5 K^{-1} (1550 nm), and 0.62 K^{-1} (808 nm), 0.61 K^{-1} (980 nm), 0.77 K^{-1} (1550 nm).

5.4. Other applications

Recently, lanthanide-based MHP NCs have been employed in several emerging applications, such as optical encoding, NIR cameras, and NIR

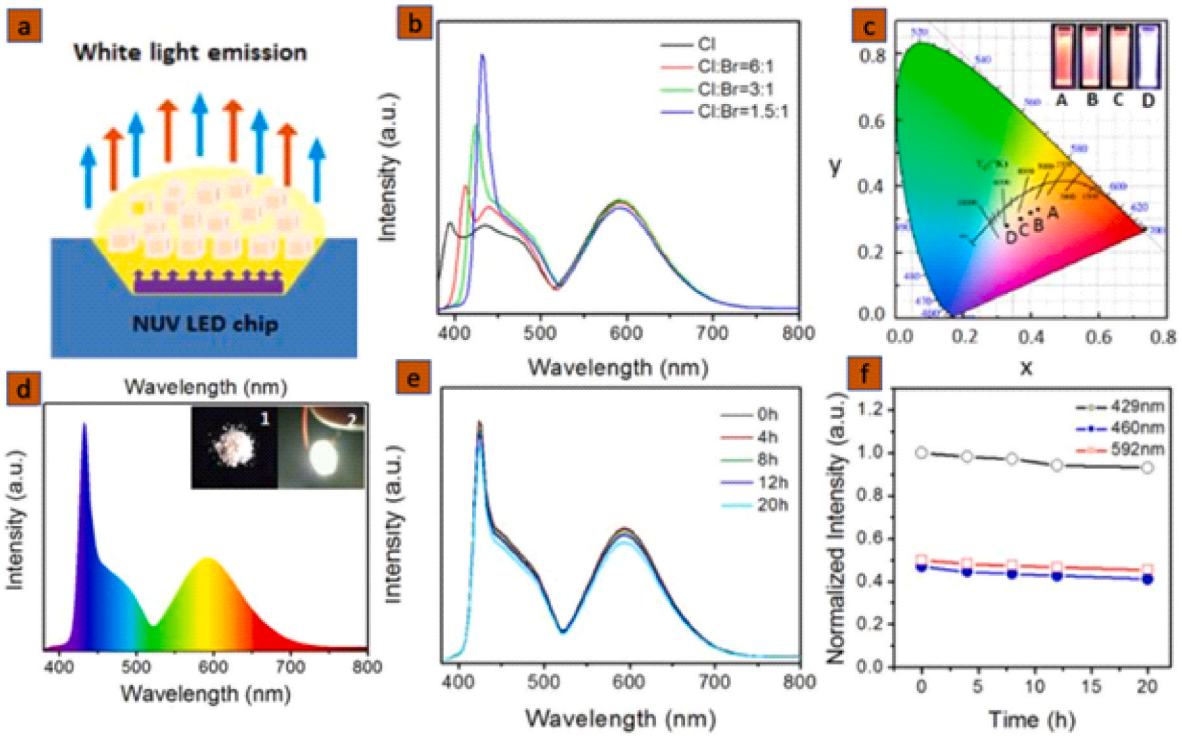

Fig. 16. (a) Schematic of WLED fabrication (b) PL spectra of 2.7% Ce^{3+}/9.1% Mn^{2+}-codoped $CsPbCl_xBr_{3-x}$ NCs. (c) CIE chromaticity coordinate of the WLED from 2.7% Ce^{3+}/9.1% Mn^{2+}- [A(0.42, 0.33), B(0.39, 0.32), C(0.37, 0.30), and D(0.33, 0.29)]. The inset is PL images of 2.7% Ce^{3+}/9.1% Mn^{2+}-codoped $CsPbCl_xBr_{3-x}$ NCs NCs under a 365 nm UV lamp. (d) PL spectra of the WLED. Inset 1 is white phosphor powder of 2.7% Ce^{3+}/9.1% Mn^{2+}-codoped $CsPbCl_xBr_{3-x}$ NCs with PS. Inset 2 is the photograph of the device operated at 3.0 V (the WLED is fabricated by coating 2.7% Ce^{3+}/9.1% Mn^{2+}-codoped $CsPbCl_xBr_{3-x}$ NCs mixed PS composites on a 365 nm chip). (e) PL spectra of the WLED as a function of time. (f) Normalized integrals of the emission peaks at 429, 460, and 592 nm for 2.7% Ce^{3+}/9.1% Mn^{2+}-codoped $CsPbCl_xBr_{3-x}$ NCs NC-mixed PS composites. Reproduced with permission from Ref. [96]. Copyright 2018, American Chemical Society.

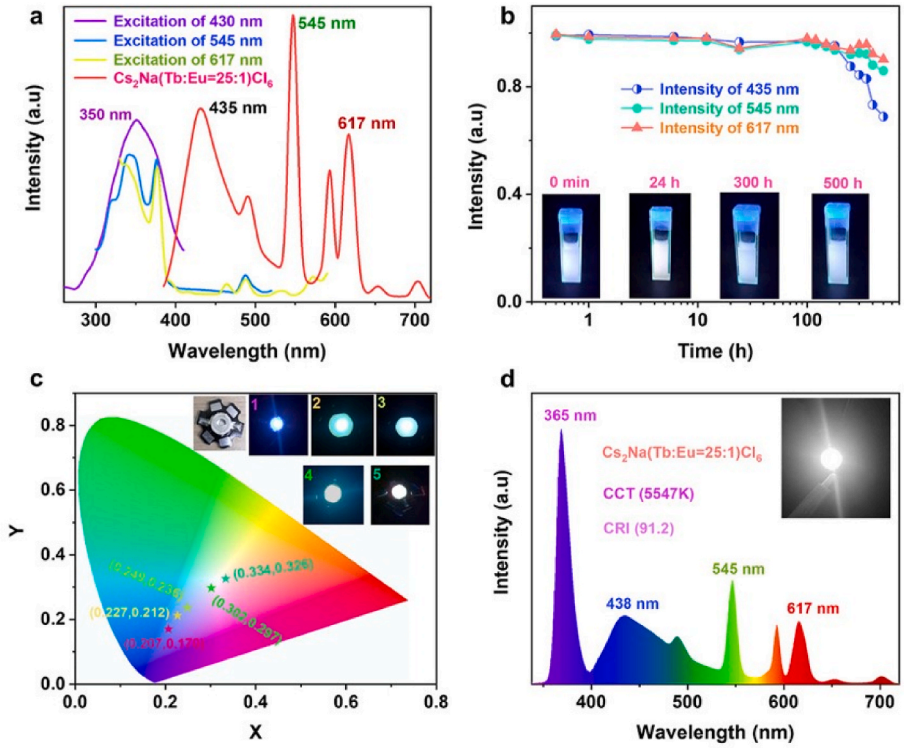

Fig. 17. White-light emission and WLED application of Cs_2NaLnX_6 NCs. a) Emission and excitation spectra of Cs_2Na (Tb:Eu = 25:1)Cl_6 NCs. b) Luminescence intensity of Cs_2Na (Tb:Eu = 25:1)Cl_6 with time changing during 500 h of continuous irradiation under 365-nm UV light along with the images of NC solution at different times. c) CIE coordinates of LEDs. The illustration shows a image of the device. d) The luminescence spectra of WLED constructed with Cs_2Na(Tb:Eu = 25:1)Cl_6 perovskite NCs. Reproduced with permission from Ref. [39]. Copyright 2023, Copyright 2016 Wiley-VCH.

Table 3
WLED fabricated with different lanthanides based MHP NCs.

WLED materials	CIE coordinates	LE (lmW^{-1})	CRI	CCT	Year
Ce:Sm:$CsPbCl_{1.8}Br_{1.2}$ + polystyrene + GaN LED	_	27	84	_	2018 [96]
Ce:Sm:$CsPbCl_3$ + polystyrene + GaN LED	_	15	70	_	2018 [96]
Ce:Eu:$CsPbCl_{1.8}Br_{1.2}$ + polystyrene + GaN LED	_	36	92	_	2018 [96]
Ce:Eu:$CsPbCl_3$ + polystyrene + GaN LED	_	23	73	_	2018 [96]
$CsPbBr_{2.2}Cl_{0.8}$: Tm^{3+}/ Mn^{2+} + 365 nm LED	(0.33, 0.34)	91			2019 [97]
Nd:$CsPbBr_3$ + UV LED + $CsPbBr_{1.2}I_{1.8}$/PMMA	(0.34, 0.33)	_	_	_	2020 [101]
Yb: $CsPbI_3$ + YAG:Ce^{3+} + GaN LED	(0.3499, 0.3542)	57	85.4	3524	2020 [95]
Eu^{3+}, Tb^{3+}:$CsPbBr_3$@glass + LED	(0.3335, 0.3413)	63.21	85.7	4945	2022 [102]
Nd:$CsPbBr_3$ + CsPbBr3 + $CsPbBr_{1.2}I_{1.8}$/PMMA	(0.34, 0.33)	_	_	_	2020 [72]
$NaYF_4$:Yb^{3+},Tm^{3+}@$NaYF_4$ + $CsPbBr_{(1-x)}I_x$ + 940 nm chip	(0.318, 0.301)	_	_	6361	2022 [100]
$CsPbBr_2I$:Gd^{3+}@glass + YAG:Ce^{3+} + INGaN LED	(0.334, 0.3386)	90.09	81.4	5434	2021 [98]
$CsPbBr_3$:Eu^{3+}/Dy^{3+} +400 nm LED	(0.3349, 0.3986),	_	78	5436	2022 [99]
Cs_2Na(Tb:Eu = 25:1)Cl_6 + 365 nm LED	(0.334, 0.320)	_	91.2	5547	2023 [39]

imaging. Stimuli-responsive optical materials such as lnathanide-based MHPs are highly effective for optical security encoding. Feng et al. reported optical encoding using Eu^{3+}-decorated $CsPbBr_3$ NCs [113]. Wang et al. demonstrated stimuli-responsive optical encoding in Yb^{3+}, Er^{3+}-doped $CsPbCl_3$ NCs [114]. I Additionally, Huang et al. reported an NIR LED with Yb^{3+}-doped $CsPbCl_3$ NCs [115].

6. Summary and perspective

This review article covers several aspects of lanthanide-based MHP NCs, including their synthesis, stability via lanthanide doping, optical properties, and applications. Moreover, this review article particularly focus on the WLEDs fabrication with lanthanide-based MHP NCs. Although this field is maturing with report of different synthesis methods, stability improvment startegies, applications in many new fields, yet, several unresolved issues require attention. We will try to summeries those issues. The MHP NCs conventionally synthesized via hot injection method, ligand assisted reprecipitation method, and thin-film method. Recently, many new synthesis techniques such as inject printing, RF magnetron sputtering, thermal evaporation, etc. have been reoprted. All these methods have advantages and disadvantages. Among these, the hot injection method is the most widely used for the synthesis of MHP NCs and thin film synthesis technique is used for solar cell application. The aim of these methods is to enhance the stability of the NCs along with high PLQY, and narrow emission band. However, long term stability of the NCs is still a major challenge for MHP NCs. However, doping MHP NCs with lanthanides significantly enhances their stability. The substitution of smaller lanthanide ions (except Gd^{3+}) in place of Pb^{2+} ions leads to lattice contraction. Therefore, the partial substitution of Pb^{2+} ions with Ln^{3+} ions enhances the formation energy. Moreover, the strong interaction between the Ln^{3+} and X^- ions reduces the trap states in the octahedra. It is worth mentioning that optically active cubic-phased $CsPbI_3$ exhibit weak stability among $CsPbX_3$, owing to its smallest tolerance factor (t) of 0.89. This results in a structural distortion in the metastable phase. In this regard, doping smaller size Ln^{3+} ions reduce the size of lattice. Thus, the distortion in octahedra reduces sugnificatly.

The optical properties of MHP NCs have been extensively studied in recent past. However, understanding some issues remains a challenge. Understanding phenomena such as phonon energy and its effect on the optoelectronic properties, phase transition, temperature-dependent PL, doping behaviors, core-shell structure of MHP, and heterostructure formation is still limited. Moreover, lanthanide doping affects the characteristic optical properties of the MHP due to lattice contraction. Therefore, the ligand field within the octahedra is enhanced, leading to an increase in the bandgap. Lanthanide doping also generates multi-modal luminescence, such as upconversion and QCL. Heterostructures or core-shell structures with lanthanide-based NCs with lead-free MHP may facilitate Fourier resonant energy transfer, which may lead to biomedical and sensing applications. Moreover, MHPs have been extensively explored for various applications, such as in solar cells, LEDs, X-ray detectors, and sensing. However, lanthanide ions in MHP have extended applications in WLEDs, NIR LEDs, NIR cameras, temperature sensors, optical security encoding, and solar cells. In particular, the 980 nm NIR luminescence from $CsPbCl_3$:Yb^{3+} have been studied for NIR imaging, solar cell. NIR luminescenece at ~1064 nm (Nd^{3+}), ~1500 nm (Er^{3+}) from lanthanide-based MHP NCs could be useful for NIR camera, communication, imaging, etc. The short wave infrared (SWIR) emission from Er^{3+} or Ho^{3+} doped $CsPbX_3$ could be useful for night vision surveillance, communication, etc. Lanthanide-based MHP have been used for temperature sensing, security encoding, etc. Moreover, lead-free lanthanide-based MHP such $CsYbI_3$, $CsEuCl_3$ and DMHPs like have opened up a new avenue in this field. In conclusion, lanthanide

Table 4
Photovoltaic parameters of lanthanide-based MHPs (characterization was conducted using solar simulator AM 1.5G with light intensity of 100 mW cm^2).

Materials	Cell Structure	J_{sc} (mA cm^{-2})	V_{oc} (V)	FE (%)	PCE (%)	Year
$CsPbBr_3$:Yb^{3+}	FTO/c-TiO_2/m-TiO_2/$CsPb0_{.97}Yb_{0.03}Br_3$/carbon	7.45	1.536	80.20	9.20	2018 [104]
$CsPbBr_3$:Er^{3+}	FTO/c-TiO_2/m-TiO_2/$CsPb0_{.97}Yb_{0.03}Br_3$ / carbon	7.46	1.563	82.80	9.66	2018 [104]
$CsPbBr_3$:Ho^{3+}	FTO/c-TiO_2/m-TiO_2/$CsPb0_{.97}Yb_{0.03}Br_3$ /carbon	7.45	1.572	83.20	9.75	2018 [104]
$CsPbBr_3$:Tb^{3+}	FTO/c-TiO_2/m-TiO_2/$CsPb0_{.97}Yb_{0.03}Br_3$ /carbon	7.47	1.588	84.80	10.06	2018 [104]
$CsPbBr_3$:Sm^{3+}	FTO/c-TiO_2/m-TiO_2/$CsPb0_{.97}Yb_{0.03}Br_3$ /carbon	7.48	1.594	85.10	10.14	2018 [104]
$CsPbI_2Br$:Eu^{3+}	FTO/c-TiO_2/mTiO_2/$CsPb_{0.95}Eu_{0.05}I_2Br$ /spiro-OMeTAD/Au	14.63	1.223	76.60	13.71	2019 [106]
$CsPbI_3$:Yb^{3+}	FTO/TiO_2/$CsPb0.95Yb_{0.05I3}$/PTB_7/MoO_3/Ag	13.25	1.250	75.00	12.42	2019 [40]
$CsPbI_2Br$:Eu^{3+}	FTO/c-TiO_2/m-TiO_2/$CsPb_{0.95}Eu_{0.05I2}Br$/spiro	14.63	1.223	76.60	13.71	2019 [106]
$MAPbI_3$:Ce^{3+}	FTO/SnO_x/$MAPBI_3$:Yb^{3+}/Spiro-OMeTAD/Ag	21.67	1.10	80.93	21.67	2020 [105]
$MAPbI_3$:Nd^{3+}	FTO/ SnO_x/$MAPBI_3$:Yb^{3+}/Spiro-OMeTAD/Ag	19.59	1.06	77.16	19.59	2020 [105]
$MAPbI_3$:Sm^{3+}	FTO/ SnO_x/$MAPBI_3$:Yb^{3+}/Spiro-OMeTAD/Ag	19.03	1.07	76.29	19.03	2020 [105]
$MAPbI_3$:Eu^{3+}	FTO/ SnO_x/$MAPBI_3$:Yb^{3+}/Spiro-OMeTAD/Ag	19.85	1.07	78.44	19.85	2020 [105]
$MAPbI_3$:Yb^{3+}	FTO/ SnO_x/$MAPBI_3$:Yb^{3+}/Spiro-OMeTAD/Ag	18.93	1.06	75.11	18.93	2020 [105]
$CsPbI_2Br$:Eu^{3+}	ITO/NiO/$CsPb_{0.995}Eu_{0.005I2}Br$/$PC_{61}BM$/Ag	15.30	1.13	70.50	12.10	2021 [107]
$CsPbBrCl_2$:Yb^{3+}	FTO/SnO_2/$MAPBI_3$-$CsPbBrCl_2$:Yb^{3+}/Spiro-OMeTAD/Ag	22.14	1.13	76.01	19.52	2022 [108]
$CsPbBrCl_2$:Ce^{3+}	FTO/SnO_2/$MAPBI_3$-$CsPbBrCl_2$:Ce^{3+}/Spiro-OMeTAD/Ag	24.34	1.16	75.84	22.15	2022 [108]
$CsPbBrCl_2$:Eu^{3+}	FTO/SnO_2/$MAPBI_3$-$CsPbBrCl_2$:Eu^{3+}/Spiro-OMeTAD/Ag	22.84	1.17	73.46	19.63	2022 [108]
$CsPbBrCl_2$:Sm^{3+}	FTO/SnO_2/$MAPBI_3$-$CsPbBrCl_2$:Sm^{3+}/Spiro-OMeTAD/Ag	23.60	1.20	79.52	22.52	2022 [108]

doping in MHP not only enhances the stability and optical properties of the NCs but also leads to multimodality. Lanthanide-based MHPs and lanthanide-based perovskite-inspired metal halides have great potential, and associated theoretical and experimental studies may unfold many new applications.

Declaration of competing Interest

The authors declare the following financial interests/personal relationships which may be considered as potential competing interests: Won Bin Im reports financial support was provided by Hanyang University. Won Bin Im reports a relationship with Korea Ministry of Trade Industry and Energy that includes: funding grants. Won Bin Im reports a relationship with National Research Foundation of Korea that includes: funding grants.

Data availability

No data was used for the research described in the article.

Acknowledgments

This work was supported by the Technology Innovation Program (KEIT-20010737) funded by the Ministry of Trade, Industry & Energy (MOTIE, Korea), the National Research Foundation of Korea (NRF) grant funded by the Korea government (MSIT) NRF-2022H1D3A3A01077343).

References

[1] J. Shamsi, A.S. Urban, M. Imran, L. De Trizio, L. Manna, Metal halide perovskite nanocrystals: synthesis, post-synthesis modifications, and their optical properties, Chem. Rev. 119 (2019) 3296–3348.
[2] S. Narayanan, N. Parikh, M.M. Tavakoli, M. Pandey, M. Kumar, A. Kalam, S. Trivedi, D. Prochowicz, P. Yadav, Metal halide perovskites for energy storage applications, Eur. J. Inorg. Chem. 2021 (2021) 1201–1212.
[3] W. Zhang, G.E. Eperon, H.J. Snaith, Metal halide perovskites for energy applications, Nat. Energy 1 (2016) 16048–16056.
[4] J.X. Lu, C.A.Z. Yan, W.J. Feng, X. Guan, K.B. Lin, Z.H. Wei, Lead-free metal halide perovskites for light emitting diodes, Ecomat 3 (2) (2021) 1–22.
[5] J.H. Han, T. Samanta, Y.M. Park, H.J. Kim, N.S.M. Viswanath, H.W. Kim, B. K. Cha, S.B. Cho, W.B. Im, Highly stable zero-dimensional lead-free metal halides for X-ray imaging, ACS Energy Lett. 8 (1) (2023) 545–552.
[6] L. Protesescu, S. Yakunin, M.I. Bodnarchuk, F. Krieg, R. Caputo, C.H. Hendon, R. X. Yang, A. Walsh, M.V. Kovalenko, Nanocrystals of cesium lead halide perovskites ($CsPbX_3$, X = Cl, Br, and I): novel optoelectronic materials showing bright emission with wide color gamut, Nano Lett. 15 (6) (2015) 3692–3696.
[7] G. Nedelcu, L. Protesescu, S. Yakunin, M.I. Bodnarchuk, M.J. Grotevent, M. V. Kovalenko, Fast anion-exchange in highly luminescent nanocrystals of cesium lead halide perovskites ($CsPbX_3$, X = Cl, Br, I), Nano Lett. 15 (8) (2015) 5635–5640.
[8] H.B. Cho, J.W. Min, H. Kim, N.S.M. Viswanath, T. Samanta, J.H. Han, Y.M. Park, S.W. Jang, W.B. Im, Three-dimensional lead halide perovskites embedded in zero-dimensional lead halide perovskites: synthesis, stability, and applications, ACS Appl. Electron. Mater. 5 (1) (2023) 66–76.
[9] G.K. Grandhi, H.J. Kim, N.S.M. Viswanath, H.B. Cho, J.H. Han, S.M. Kim, W. B. Im, Strategies for improving luminescence efficiencies of blue-emitting metal halide perovskites, J. Korean Ceram. Soc. 58 (2021) 28–41.
[10] V.M. Goldschmidt, Die Gesetze der Krystallochemie Naturwissenschaften 14 (1926) 477–485.
[11] A. Dey, J.Z. Ye, A. De, E. Debroye, S.K. Ha, E. Bladt, A.S. Kshirsagar, Z.Y. Wang, J. Yin, Y. Wang, L.N. Quan, F. Yan, M.Y. Gao, X.M. Li, J. Shamsi, T. Debnath, M. H. Cao, M.A. Scheel, S. Kumar, J.A. Steele, M. Gerhard, L. Chouhan, K. Xu, X. G. Wu, Y.X. Li, Y.N. Zhang, A. Dutta, C. Han, I. Vincon, A.L. Rogach, A. Nag, A. Samanta, B.A. Korgel, C.J. Shih, D.R. Gamelin, D.H. Son, H.B. Zeng, H. Z. Zhong, H.D. Sun, H.V. Demir, I.G. Scheblykin, I. Mora-Sero, J.K. Stolarczyk, J. Z. Zhang, J. Feldmann, J. Hofkens, J.M. Luther, J. Perez-Prieto, L. Li, L. Manna, M.I. Bodnarchuk, M.V. Kovalenko, M.B.J. Roeffaers, N. Pradhan, O. F. Mohammed, O.M. Bakr, P.D. Yang, P. Muller-Buschbaum, P.V. Kamat, Q. L. Bao, Q. Zhang, R. Krahne, R.E. Galian, S.D. Stranks, S. Bals, V. Biju, W. A. Tisdale, Y. Yan, R.L.Z. Hoye, L. Polavarapu, State of the art and prospects for halide perovskite nanocrystals, ACS Nano 15 (2021) 10775–10981.
[12] H.W. Liu, Z.N. Wu, H. Gao, J.R. Shao, H.Y. Zou, D. Yao, Y. Liu, H. Zhang, B. Yang, One-step preparation of cesium lead halide $CsPbX_3$ (X = Cl, Br, and I) perovskite nanocrystals by microwave irradiation, ACS Appl. Mater. Interfaces 9 (49) (2017) 42919–44292.
[13] S. Ahmed, S. Lahkar, P. Saikia, D. Mohanta, J. Das, S.K. Dolui, Stable and highly luminescent $CsPbX_3$(X= Br, Br/Cl) perovskite quantum dot embedded into Zinc (II) imidazole-4,5-dicarboxylate metal organic framework as a luminescent probe for metal ion detection, Mater. Chem. Phys. 295 (2013) 127093–127110.
[14] X.C. Liu, P. Zeng, S.H. Chen, T.A. Smith, M.Z. Liu, Charge transfer dynamics at the interface of $CsPbX_3$ perovskite nanocrystal-acceptor complexes: a femtosecond transient absorption spectroscopy study, Laser Photon. Rev. 16 (12) (2022) 2200280–2200298.
[15] W.L. Song, B. Zhang, W.L. Zhou, J.L. Zhang, S.X. Lian, L.P. Yu, Suppression of thermal quenching for $CsPbX_3$ (X = Cl, Br, and I) quantum dots via the hollow structure of $SrTiO_3$ and light-emitting diode applications, Inorg. Chem. 61 (49) (2022) 19899–19906.
[16] J. Huang, Y. Yuan, Y. Shao, Y. Yan, Understanding the physical properties of hybrid perovskites for photovoltaic applications, Nat. Rev. Mater. 2 (7) (2017) 17042–17061.
[17] K. Leng, W. Fu, Y.P. Liu, M. Chhowalla, K.P. Loh, From bulk to molecularly thin hybrid perovskites, Nat. Rev. Mater. 5 (7) (2020) 482–500.
[18] I. Deretzis, E. Smecca, G. Mannino, A. La Magna, T. Miyasaka, A. Alberti, Stability and degradation in hybrid perovskites: is the glass half-empty or half-full? J. Phys. Chem. Lett. 9 (11) (2018) 3000–3007.
[19] H. Liao, S.B. Guo, S. Cao, L. Wang, F.M. Gao, Z.B. Yang, J.J. Zheng, W.Y. Yang, A general strategy for in situ growth of all-inorganic $CsPbX_3$ (X = Br, I, and Cl) perovskite nanocrystals in polymer fibers toward significantly enhanced water/thermal stabilities, Adv. Opt. Mater. 6 (15) (2018), 1800346-1800346.
[20] K. Xing, S. Cao, X. Yuan, R.S. Zeng, H.B. Li, B.S. Zou, J.L. Zhao, Thermal and photo stability of all inorganic lead halide perovskite nanocrystals, Phys. Chem. Chem. Phys. 23 (32) (2021) 17113–17128.
[21] Z.H. Hu, T. Chen, Y.Q. Xu, W.H. Jiang, Z.X. Xie, Surface coating strategy: from improving the luminescence stability to lighting and display applications of all-inorganic cesium lead halide perovskite nanocrystals, Prog. Chem. 33 (9) (2021) 1614–1626.
[22] J. Sun, J. Yang, J.I. Lee, J.H. Cho, M.S. Kang, Lead-free perovskite nanocrystals for light-emitting devices, J. Phys. Chem. Lett. 9 (7) (2018) 1573–1583.
[23] T. Samanta, N.S.M. Viswanath, S.W. Jang, J.W. Min, H.B. Cho, J.H. Han, W.B. Im, Thermally stable self-trapped assisted single-component white light from lead-free zero-dimensional metal halide nanocrystals, Adv. Opt. Mater. (2023) 2202744–2202751.
[24] J.H. Han, T. Samanta, Y.M. Park, H. Bin Cho, J.W. Min, S.J. Hwang, S.W. Jang, W. B. Im, Effect of self-trapped excitons in the optical properties of manganese-alloyed hexagonal-phased metal halide perovskite, Chem. Eng. J. 450 (2022) 138325–138334.
[25] T.A.D. Carvalho, L.F. Magalhaes, C.I.D. Santos, T.A.Z. de Freitas, B.R.C. Vale, A.F. V. da Fonseca, M.A. Schiavon, Lead-free metal halide perovskite nanocrystals: from fundamentals to applications, Chem. Eur J. 29 (4) (2023) 1–18.
[26] R. Marin, D. Jaque, R. Marin, D. Jaque, Doping lanthanide ions in colloidal semiconductor nanocrystals for brighter photoluminescence, Chem. Rev. 121 (3) (2021) 1425–1462.
[27] K.M. Du, J. Feng, X. Gao, H.J. Zhang, Nanocomposites based on lanthanide-doped upconversion nanoparticles: diverse designs and applications, Light Sci. Appl. 11 (1) (2022) 1–23.
[28] D. Sarkar, B. Meesaragandla, T. Samanta, V. Mahalingam, A greener approach towards making highly luminescent $Ln(^{3+})$-doped $NaYF_4$ nanoparticles with ligand-assisted phase control, ChemistrySelect 1 (15) (2016) 4785–4793.
[29] T. Samanta, C. Hazra, A.E. Praveen, S. Ganguli, V. Mahalingam, Synthesis of hexagonal-phase Eu^{3+}-doped GdF_3 nanocrystals above room temperature by controlling the viscosity of the solvents, Eur. J. Inorg. Chem. (6) (2016) 802–807.
[30] C. Hazra, T. Samanta, S. Ganguli, V. Mahalingam, Strong UV emission from colloidal Eu^{2+}-doped $BaSO_4$ nanoparticles: a material for enhancing the photocatalytic activity of carbon dots, ChemistrySelect 2 (21) (2017) 5970–5977.
[31] J.C.G. Bunzli, C. Piguet, Taking advantage of luminescent lanthanide ions, Chem. Soc. Rev. 34 (12) (2005) 1048–1077.
[32] W.J. Mir, T. Sheikh, H. Arfin, Z.G. Xia, A. Nag, Lanthanide doping in metal halide perovskite nanocrystals: spectral shifting, quantum cutting and optoelectronic applications, NPG Asia Mater. 12 (1) (2020) 1–9.
[33] S. Kachhap, S. Singh, A.K. Singh, S.K. Singh, Lanthanide-doped inorganic halide perovskites ($CsPbX_3$): novel properties and emerging applications, J. Mater. Chem. C 10 (10) (2022) 3647–3676.
[34] A.G. Bispo, A.J.D. Morais, C.M.S. Calado, I.O. Mazali, F.A. Sigoli, Lanthanide-doped luminescent perovskites: a review of synthesis, properties, and applications, J. Lumin. 252 (2022) 119406–119422.
[35] Z.C. Li, B.L. Zhang, Z.H. Zhang, J.C. Bunzli, A.B. Yusoff, Y.Y. Noh, P. Gao, Vitamin needed: lanthanides in optoelectronic applications of metal halide perovskites, Mat. Sci. Eng. R. 152 (2023) 100710–100745.
[36] K.M. Walsh, K. Pressler, M.J. Crane, D.R. Gamelin, Ferromagnetism and spin-polarized luminescence in lead-free $CsEuCl_3$ perovskite nanocrystals and thin films, ACS Nano 16 (2) (2022) 2569–2576.
[37] J. Huang, T. Lei, M. Siron, Y. Zhang, S. Yu, F. Seeler, A. Dehestani, L.N. Quan, K. Schierle-Arndt, P. Yang, Lead-free cesium europium halide perovskite nanocrystals, Nano Lett. 20 (5) (2020) 3734–3739.
[38] B.J. Moon, S.J. Kim, S. Lee, A. Lee, H. Lee, D.S. Lee, T.W. Kim, S.K. Lee, S. Bae, S. H. Lee, Rare-earth-element-ytterbium-substituted lead-free inorganic perovskite nanocrystals for optoelectronic applications, Adv. Mater. 31 (33) (2019) 1901716–1901723.
[39] L. Sun, B. Dong, J. Sun, Y. Wang, R. Sun, S. Hu, B. Zhou, W. Xu, X. Bai, L. Xu, D. Zhou, H. Song, Fabrication, Optical Property, and White LED Application of

Novel Lanthanide-Based Family Cs_2NaLnX_6 (X = Cl, Br, I) Perovskite Nanomaterials, Laser Photonics Rev., 2023, 2300045-230058.
[40] C.B. Murray, D.J. Norris, M.G. Bawendi, Synthesis and characterization of nearly monodisperse cde (E = S, Se, Te) semiconductor nanocrystallites, J. Am. Chem. Soc. 115 (19) (1993) 8706–8715.
[41] W.W. Yu, X. Peng, Formation of high-quality CdS and other II-VI semiconductor nanocrystals in noncoordinating solvents: tunable reactivity of monomers, Angew. Chem., Int. Ed. 46 (15) (2007) 2559–2563.
[42] C.R. Bullen, P. Mulvaney, Nucleation and growth kinetics of CdSe nanocrystals in octadecene, Nano Lett. 4 (12) (2004) 2303–2307.
[43] B.W. Zhang, L. Goldoni, C. Lambruschini, L. Moni, M. Imran, A. Pianetti, V. Pinchetti, S. Brovelli, L. De Trizio, L. Manna, Stable and size tunable $CsPbBr_3$ nanocrystals synthesized with oleylphosphonic acid, Nano Lett. 20 (12) (2020) 8847–8853.
[44] A.Z. Pan, B. He, X.Y. Fan, Z.K. Liu, J.J. Urban, A.P. Alivisatos, L. He, Y. Liu, Insight into the ligand-mediated synthesis of colloidal CsPbBr3 perovskite nanocrystals: the role of organic acid, base, and cesium precursors, ACS Nano 10 (2016) 7943–7954.
[45] D. Zhou, D. Liu, G. Pan, X. Chen, D. Li, W. Xu, X. Bai, H. Song, Cerium and ytterbium codoped halide perovskite quantum dots: a novel and efficient downconverter for improving the performance of silicon solar cells, Adv. Mater. 29 (42) (2017) 1704149–1704155.
[46] G.C. Pan, X. Bai, D.W. Yang, X. Chen, P.T. Jing, S.N. Qu, L.J. Zhang, D.L. Zhou, J. Y. Zhu, W. Xu, B. Dong, H.W. Song, Doping lanthanide into perovskite nanocrystals: highly improved and expanded optical properties, Nano Lett. 17 (12) (2017) 8005–8011.
[47] X. Zhang, Y. Zhang, X. Zhang, W. Yin, Y. Wang, H. Wang, M. Lu, Z. Li, Z. Gu, W.Y. J. William, Yb^{3+} and Yb^{3+}/Er^{3+} doping for near-infrared emission and improved stability of $CsPbCl_3$ nanocrystals, J. Mater. Chem. C 6 (37) (2018) 10101–10105.
[48] H. Huang, R. Li, S. Jin, Z. Li, P. Huang, J. Hong, S. Du, W. Zheng, X. Chen, D. Chen, Interfaces, Ytterbium-doped $CsPbCl_3$ quantum cutters for near-infrared light-emitting diodes, ACS Appl. Mater. 13 (29) (2021) 34561–34571.
[49] A. Wang, X. Yan, M. Zhang, S. Sun, M. Yang, W. Shen, X. Pan, P. Wang, Z. Deng, Controlled synthesis of lead-free and stable perovskite derivative Cs_2SnI_6 nanocrystals via a facile hot-injection process, Chem. Mater. 28 (22) (2016) 8132–8140.
[50] Y. Yu, W. Zhou, C. Li, P. Han, H. Li, K. Zhao, Tb^{3+} and Bi^{3+} Co-doping of lead-free $Cs_2NaInCl_6$ double perovskite nanocrystals for tailoring optical properties, Nanomaterials 13 (3) (2023) 549–558.
[51] J.S. Yao, J. Ge, B.N. Han, K.H. Wang, H.B. Yao, H.L. Yu, J.H. Li, B.S. Zhu, J. Z. Song, C.J. Chen, Ce^{3+}-doping to modulate photoluminescence kinetics for efficient $CsPbBr_3$ nanocrystals based light-emitting diodes, J. Am. Chem. Soc. 140 (10) (2018) 3626–3634.
[52] Q. Li, Y. Liu, P. Chen, J. Hou, Y. Sun, G. Zhao, N. Zhang, J. Zou, J. Xu, Y. Fang, Excitonic luminescence engineering in tervalent-europium-doped cesium lead halide perovskite nanocrystals and their temperature-dependent energy transfer emission properties, J. Phys. Chem. C 122 (50) (2018) 29044–29050.
[53] J. Luo, L. Yang, Z. Tan, W. Xie, Q. Sun, J. Li, P. Du, Q. Xiao, L. Wang, X. Zhao, Efficient blue light emitting diodes based on europium halide perovskites, Adv. Mater. 33 (38) (2021) 2101903–2101912.
[54] M. Jin, Z. Zeng, H. Fu, S. Wang, Z. Yin, X. Zhai, Q. Zhang, Y. Du, Strain-negligible Eu^{2+} doping enabled color-tunable harsh condition-resistant perovskite nanocrystals for superior LightEmitting diodes, Nano Letters JACS Au (2022) 216–226.
[55] X. Shen, Z. Wang, C. Tang, X. Zhang, B.R. Lee, X. Li, D. Li, Y. Zhang, J. Hu, D. Zhao, Strain-Negligible Eu^{2+} Doping Enabled Color-Tunable Harsh Condition-Resistant Perovskite Nanocrystals for Superior LightEmitting Diodes Nano Letters, 2022.
[56] R. Sun, P. Lu, D. Zhou, W. Xu, N. Ding, H. Shao, Y. Zhang, D. Li, N. Wang, X. Zhuang, Samarium-doped metal halide perovskite nanocrystals for single-component electroluminescent white light-emitting diodes, ACS Energy Lett. 5 (7) (2020) 2131–2139.
[57] W. Xia, Z. Ren, Z. Zheng, C. Luo, J. Li, W. Ma, X. Zhou, Y.J.N. Chen, Highly stable lanthanide-doped $CsPbI_3$ perovskite nanocrystals with near-unity quantum yield for efficient red light-emitting diodes, Nanoscale 15 (3) (2023) 1109–1118.
[58] T. Chiba, J. Sato, S. Ishikawa, Y. Takahashi, H. Ebe, S. Sumikoshi, S. Ohisa, J. Kido, Interfaces, Neodymium chloride-doped perovskite nanocrystals for efficient blue light-emitting devices, ACS Appl. Mater. 12 (48) (2020) 53891–53898.
[59] Y. Mahor, W.J. Mir, A. Nag, Synthesis and near-infrared emission of Yb-doped $Cs_2AgInCl_6$ double perovskite microcrystals and nanocrystals, J. Phys. Chem. C 123 (25) (2019) 15787–15793.
[60] S. Wang, J. Qi, S.V. Kershaw, A.L.J. Rogach, Co-doping of cerium and bismuth into lead-free double perovskite $Cs_2AgInCl_6$ nanocrystals results in improved photoluminescence efficiency, ACS Nanoscience Au 2 (2) (2021) 93–101.
[61] Y. Xie, B. Peng, I. Bravić, Y. Yu, Y. Dong, R. Liang, Q. Ou, B. Monserrat, S. Zhang, Highly efficient blue-emitting $CsPbBr_3$ perovskite nanocrystals through neodymium doping, Adv. Sci. 7 (20) (2020) 2001698–2001707.
[62] H. Arfin, J. Kaur, T. Sheikh, S. Chakraborty, A. Nag, Bi^{3+}-Er^{3+} and Bi^{3+}-Yb^{3+} codoped $Cs_2AgInCl_6$ double perovskite near-infrared emitters, Angew. Chem., Int. Ed. Engl. 59 (28) (2020) 11307–11311.
[63] Y. Zhu, J. Zhu, H. Song, J. Huang, Z. Lu, G. Pan, Samarium doping improves luminescence efficiency of $Cs_3Bi_2Br_9$ perovskite quantum dots enabling efficient white light-emitting diodes, J. Rare Earths 39 (4) (2021) 374–379.
[64] J. Duan, Y. Zhao, X. Yang, Y. Wang, B. He, Q. Tang, Lanthanide ions doped $CsPbBr_3$ halides for HTM-free 10.14%-efficiency inorganic perovskite solar cell with an ultrahigh open-circuit voltage of 1.594 V, Adv. Energy Mater. 8 (31) (2018) 1802346–1802355.
[65] A. Suzuki, K. Kishimoto, T. Oku, M. Okita, S. Fukunishi, T.J.S.M. Tachikawa, Additive effect of lanthanide compounds into perovskite layer on photovoltaic properties and electronic structures, Synth. Met. 287 (2022) 117092–117103.
[66] N. Ding, D. Zhou, G. Pan, W. Xu, X. Chen, D. Li, X. Zhang, J. Zhu, Y. Ji, H.J.A.S. C. Song, Europium-doped lead-free $Cs_3Bi_2Br_9$ perovskite quantum dots and ultrasensitive Cu^{2+} detection, ACS Sustain. Chem. Eng. 7 (9) (2019) 8397–8404.
[67] T.A. de Souza Carvalho, L.F. Magalhaes, C.I. do Livramento Santos, T.A.Z. de Freitas, B.R. Carvalho Vale, A.F. Vale da Fonseca, M.A. Schiavon, Lead-free metal halide perovskite nanocrystals: from fundamentals to applications, Chem. Eur J. 29 (4) (2023) 202202518–202202536.
[68] J. Duan, Y. Zhao, X. Yang, Y. Wang, B. He, Q. Tang, Lanthanide ions doped $CsPbBr_3$ halides for HTM-free 10.14%-efficiency inorganic perovskite solar cell with an ultrahigh open-circuit voltage of 1.594 V, Adv. Energy Mater. 8 (31) (2018) 1802346–1802355.
[69] H.R. Peng, M.L. Cai, J.Y. Zhou, Y. Yang, X.H. Ding, Y. Tao, G. Wu, X.P. Liu, J. H. Pan, S.Y. Dai, Structurally reinforced all-inorganic $CsPbI_2Br$ perovskite by nonionic polymer via coordination and hydrogen bonds, Sol Rrl 4 (9) (2020).
[70] E. Akman, T. Ozturk, W.C. Xiang, F. Sadegh, D. Prochowicz, M.M. Tavakoli, P. Yadav, M. Yilmaz, S. Akin, The effect of B-site doping in all-inorganic $CsPbI_xBr_{3-x}$ absorbers on the performance and stability of perovskite photovoltaics, Energy Environ. Sci. 16 (2022) 372–403.
[71] W. Xia, Z. Ren, Z. Zheng, C. Luo, J. Li, W. Ma, X. Zhou, Y. Chen, Highly stable lanthanide-doped $CsPbI_3$ perovskite nanocrystals with near-unity quantum yield for efficient red light-emitting diodes, Nanoscale 15 (3) (2023) 1109–1118.
[72] Y. Xie, B. Peng, I. Bravic, Y. Yu, Y. Dong, R. Liang, Q. Ou, B. Monserrat, S. Zhang, Highly efficient blue-emitting $CsPbBr_3$ perovskite nanocrystals through neodymium doping, Adv. Sci. 7 (20) (2020) 2001698–2001707.
[73] K.Y. Xu, D.J. Chen, D.C. Huang, H.M. Zhu, Thermally stable emission from Yb^{3+}-doped $CsPbCl_3$ nanocrystals, J. Lumin. 240 (2021) 118464–118469.
[74] J.S. Manser, J.A. Christians, P.V. Kamat, Intriguing optoelectronic properties of metal halide perovskites, Chem.l Rev. 116 (21) (2016) 12956–13008.
[75] Y.T. Dong, T. Qiao, D. Kim, D. Parobek, D. Rossi, D.H. Son, Precise control of quantum confinement in cesium lead halide perovskite quantum dots via thermodynamic equilibrium, Nano Lett. 18 (6) (2018) 3716–3722.
[76] G.E. Eperon, S.D. Stranks, C. Menelaou, M.B. Johnston, L.M. Herz, H.J. Snaith, Formamidinium lead trihalide: a broadly tunable perovskite for efficient planar heterojunction solar cells, Energy Environ. Sci. 7 (3) (2014) 982–988.
[77] Y.P. Fu, H.M. Zhu, J. Chen, M.P. Hautzinger, X.Y. Zhu, S. Jin, Metal halide perovskite nanostructures for optoelectronic applications and the study of physical properties, Nat. Rev. Mater. 4 (3) (2019) 169–188.
[78] J. Pan, Y.Q. Shang, J. Yin, M.D. Bastiani, W. Peng, I. Dursun, L. Sinatra, A.M. El-Zohry, M.N. Hedhili, A.H. Emwas, O.F. Mohammed, Z.J. Ning, O.M. Bakr, Bidentate ligand-passivated $CsPbI_3$ perovskite nanocrystals for stable near-unity photoluminescence quantum yield and efficient red light-emitting diodes, J. Am. Chem. Soc. 140 (2) (2018) 562–565.
[79] D.A. Egger, A. Bera, D. Cahen, G. Hodes, T. Kirchartz, L. Kronik, R. Lovrincic, A. M. Rappe, D.R. Reichman, O. Yaffe, What remains unexplained about the properties of halide perovskites? Adv. Mater. 30 (20) (2018) 1800691–1800702.
[80] I. Levchuk, A. Osvet, X.F. Tang, M. Brandl, J.D. Perea, F. Hoegl, G.J. Matt, R. Hock, M. Batentschuk, C.J. Brabec, Brightly luminescent and color-tunable Formamidinium lead halide perovskite $FAPbX_3$(X = Cl, Br, I) colloidal nanocrystals, Nano Lett. 17 (2017) 2765–2770.
[81] D. Sarkar, S. Ganguli, T. Samanta, V. Mahalingam, Design of lanthanide-doped colloidal nanocrystals: applications as phosphors, Sensors, and Photocatalysts, Langmuir 35 (19) (2019) 6211–6230.
[82] Y.H. Kim, P. Arunkumar, B.Y. Kim, S. Unithrattil, E. Kim, S.H. Moon, J.Y. Hyun, K.H. Kim, D. Lee, J.S. Lee, W.B. Im, A zero-thermal-quenching phosphor, Nat. Mater. 16 (5) (2017) 543–550.
[83] W.B. Im, N.N. Fellows, S.P. DenBaars, R. Seshadri, Y.I. Kim, $LaSr_2AlO_5$, a versatile host compound for Ce^{3+}-based yellow phosphors: structural tuning of optical properties and use in solid-state white lighting, Chem. Mater. 21 (13) (2009) 2957–2966.
[84] F. Wang, X.G. Liu, Recent advances in the chemistry of lanthanide-doped upconversion nanocrystals, Chem. Soc. Rev. 38 (4) (2009) 976–989.
[85] F. Wang, D. Banerjee, Y.S. Liu, X.Y. Chen, X.G. Liu, Upconversion nanoparticles in biological labeling, imaging, and therapy, Analyst 135 (8) (2010) 1839–1854.
[86] X.Y. Huang, S.Y. Han, W. Huang, X.G. Liu, Enhancing solar cell efficiency: the search for luminescent materials as spectral converters, Chem. Soc. Rev. 42 (1) (2013) 173–201.
[87] Y. Zhou, J. Chen, O.M. Bakr, H.T. Sun, Metal-doped lead halide perovskites: synthesis, properties, and optoelectronic applications, Chem. Mater. 30 (19) (2018) 6589–6613.
[88] R.T. Wegh, H. Donker, K.D. Oskam, A. Meijerink, Visible quantum cutting in $LiGdF_4$: Eu^{3+} through downconversion, Science 283 (5402) (1999) 663–666.
[89] D.L. Zhou, D.L. Liu, G.C. Pan, X. Chen, D.Y. Li, W. Xu, X. Bai, H.W. Song, Cerium and ytterbium codoped halide perovskite quantum dots: a novel and efficient downconverter for improving the performance of silicon solar cells, Adv. Mater. 29 (42) (2017) 1704149–1704155.
[90] T.J. Milstein, K.T. Kluherz, D.M. Kroupa, C.S. Erickson, J.J. De Yoreo, D. R. Gamelin, Anion exchange and the quantum-cutting energy threshold in ytterbium-doped $CsPb(Cl_{1-x}Br_x)_3$ perovskite nanocrystals, Nano Lett. 19 (3) (2019) 1931–1937.

[91] X. Li, S. Duan, H. Liu, G. Chen, Y. Luo, H. Agren, Mechanism for the extremely efficient sensitization of Yb^{3+}Luminescence in $CsPbCl_3$ nanocrystals, J. Phys. Chem. Lett. 10 (2019) 487–492.
[92] S.X. Yang, C.H. Bi, J.J. Tian, Highly pure white light-emitting single-component perovskite colloidal quantum dots, J. Phys. Chem. C 125 (34) (2021) 18810–18816.
[93] B. Zhou, Z.X. Liu, S.F. Fang, H.Z. Zhong, B.B. Tian, Y. Wang, H.N. Li, H.L. Hu, Y. M. Shi, Efficient white photoluminescence from self-trapped excitons in Sb^{3+}/Bi^{3+}-codoped $Cs_2NaInCl_6$ double perovskites with tunable dual-emission, ACS Energy Lett. 6 (9) (2021) 3343–5331.
[94] H.S. Jang, W.B. Im, D.C. Lee, D.Y. Jeon, S.S. Kim, Enhancement of red spectral emission intensity of $Y_3Al_5O_{12}$: Ce^{3+} phosphor via Pr co-doping and Tb substitution for the application to white LEDs, J. Lumin. 126 (2) (2007) 371–377.
[95] L. Yuan, L. Zhou, W. Xiang, X. Liang, Enhanced stability of red-emitting $CsPbI_3$: Yb^{3+}nanocrystal glasses: a potential luminescent material, J. Non-Cryst. Solids 545 (2020) 120232–120239.
[96] G. Pan, X. Bai, W. Xu, X. Chen, D. Zhou, J. Zhu, H. Shao, Y. Zhai, B. Dong, L. Xu, H. Song, Impurity ions codoped cesium lead halide perovskite nanocrystals with bright white light emission toward ultraviolet-white light-emitting diode, ACS Appl. Mater. Interfaces 10 (45) (2018) 39040–39048.
[97] C. Luo, W. Li, J. Fu, W. Yang, Constructing gradient energy levels to promote exciton energy transfer for photoluminescence controllability of all-inorganic perovskites and application in single-component WLEDs, Chem. Mater. 31 (15) (2019) 5616–5624.
[98] Q. He, Y. Zhang, Y. Yu, Y. Chen, M. Jin, E. Mei, X. Liang, L. Zhai, W. Xiang, Ultrastable Gd^{3+} doped $CsPbBrI_2$ nanocrystals red glass for high efficiency WLEDs, Chem. Eng. J. 411 (2021), 128530-125537.
[99] E. Erol, N. Vahedigharehchopogh, U. Ekim, N. Uza, M. Çelikbilek Ersundu, A. E. Ersundu, Ultra-stable Eu^{3+}/Dy^{3+} co-doped $CsPbBr_3$ quantum dot glass nanocomposites with tunable luminescence properties for phosphor-free WLED applications, J. Alloys Compd. 909 (2022) 164650–164658.
[100] V. Naresh, V.N.K.B. Adusumalli, Y.I. Park, N. Lee, NIR triggered $NaYF_4$:Yb^{3+},Tm^{3+}@$NaYF_4$/$CsPb(Br_{1-x}/I_x)_3$ composite for up-converted white-light emission and dual-model anti-counterfeiting applications, Mater. Today Chem. 23 (2022) 100752–100765.
[101] M.A. Padhiar, M. Wang, Y. Ji, Z. Yang, A.S. Bhatti, Tuning optical properties of $CsPbBr_3$ by mixing Nd^{3+} trivalent lanthanide halide cations for blue light emitting devices, Nanotechnology 33 (17) (2022) 175202–175233.
[102] Y. Cheng, C. Shen, L. Shen, W. Xiang, X. Liang, Tb^{3+}, Eu^{3+} Co-doped $CsPbBr_3$ QDs glass with highly stable and luminous adjustable for white LEDs, ACS Appl. Mater. Interfaces 10 (25) (2018) 21434–21444.
[103] J.J. Yoo, G. Seo, M.R. Chua, T.G. Park, Y.L. Lu, F. Rotermund, Y.K. Kim, C. S. Moon, N.J. Jeon, J.P. Correa-Baena, V. Bulovic, S.S. Shin, M.G. Bawendi, J. Seo, Efficient perovskite solar cells via improved carrier management, Nature 590 (7847) (2021) 587–593.
[104] J. Duan, Y. Zhao, X. Yang, Y. Wang, B. He, Q. Tang, Lanthanide ions doped $CsPbBr_3$ halides for HTM-free 10.14%-efficiency inorganic perovskite solar cell with an ultrahigh open-circuit voltage of 1.594 V, Adv. Energy Mater. 8 (31) (2018) 1802346–1802355.
[105] Z. Song, W. Xu, Y. Wu, S. Liu, W. Bi, X. Chen, H. Song, Incorporating of lanthanides ions into perovskite film for efficient and stable perovskite solar cells, Small 16 (40) (2020) 2001770–2001781.
[106] W.C. Xiang, Z.W. Wang, D.J. Kubicki, W. Tress, J.S. Luo, D. Prochowicz, S. Akin, L. Emsley, J.T. Zhou, G. Dietler, M. Gratzel, A. Hagfeldt, Europium-doped $CsPbI_2Br$ for stable and highly efficient inorganic perovskite solar cells, Joule 3 (1) (2019) 205–214.
[107] L.B. Chen, W. Wu, J.P. Wang, Z.Y. Qian, R.G. Liu, Y.Y. Niu, Y.H. Chen, X.J. Xie, H. Zhang, Lanthanide stabilized all-inorganic CsPbI2Br perovskite solar cells with superior thermal resistance, ACs Appl. Energ. Mater. 4 (4) (2021) 3937–3944.
[108] X. Zhuang, R. Sun, D. Zhou, S. Liu, Y. Wu, Z. Shi, Y. Zhang, B. Liu, C. Chen, D. Liu, H. Song, Synergistic effects of multifunctional lanthanides doped $CsPbBrCl_2$ quantum dots for efficient and stable $MAPbI_3$ perovskite solar cells, Adv. Funct. Mater. 32 (18) (2022) 2110346–2110360.
[109] M. Jia, Z. Sun, M. Zhang, H. Xu, Z. Fu, What determines the performance of lanthanide-based ratiometric nanothermometers? Nanoscale 12 (40) (2020) 20776–20785.
[110] Y. Zhang, J. Liu, H. Zhang, Q. He, X. Liang, W. Xiang, Ultra-stable Tb^{3+}: $CsPbI_3$ nanocrystal glasses for wide-range high-sensitivity optical temperature sensing, J. Eur. Ceram. 40 (15) (2020) 6023–6030.
[111] G. Yao, S. Li, D. Valiev, Q. Chen, Y. Hu, L. Jia, S. Stepanov, Y. Zhou, C. Li, Z. Su, F. Zeng, Structural, spectroscopic and temperature characterizations of Dy^{3+}-doped $CsPbBr_3$ quantum dots in borogermanate glass-ceramics, Opt. Mater. 122 (2021) 111711–111719.
[112] C. Zhao, Y. Gao, D. Zhou, F. Zhu, J. Chen, J. Qiu, High-efficiency dual-mode luminescence of metal halide perovskite $Cs_3Bi_2Cl_9$:Er^{3+} and its use in optical temperature measurement with high sensitivity, J. Alloys Compd. 944 (2023) 169134–169145.
[113] P.F. Feng, X.X. Yang, X.X. Feng, G.D. Zhao, X.C. Li, J. Cao, Y. Tang, C.H. Yan, Highly stable perovskite quantum dots modified by europium complex for dual-responsive optical encoding, ACS Nano 15 (4) (2021) 6266–6275.
[114] S.X. Wang, J.W. Zhu, H. Huang, J.D. Lin, C.B. Yang, S.X. Liao, F. Huang, D. Q. Chen, Erasable glass-stabilized perovskite quantum dots for NIR-laser-stimuli-responsive optical security, Cell Rep. Phys. Sci. 3 (3) (2022) 100794–100808.
[115] H. Huang, R.F. Li, S.L. Jin, Z.F. Li, P. Huang, J.Q. Hong, S.W. Du, W. Zheng, X. Y. Chen, D.Q. Chen, Ytterbium-doped $CsPbCl_3$ quantum cutters for near-infrared light-emitting diodes, ACS Appl. Mater. Interfaces 13 (29) (2021) 34561–34571.